Piezoelectric single crystal based one-dimensional phased array for breast tissue imaging

by

Wenya Du

B.S, North China Institute of Aerospace Engineering (2010)

M.Eng., Auburn University (2014)

Submitted to the Program in Media Arts and Sciences, School of Architecture and Planning, in

partial fulfillment of the requirements for the degree of

Master of Science

at the

Massachusetts Institute of Technology (MIT)

September 2024

© 2024 Wenya Du. All rights reserved

The author hereby grants to MIT a nonexclusive, worldwide, irrevocable, royalty-free license to exercise any and all rights under copyright, including to reproduce, preserve, distribute and publicly display copies of the thesis, or release the thesis under an open-access license.

Authored by: Wenya Du

Program in Media Arts and Sciences

August 15, 2024

Certified by: Canan Dagdeviren

Associate Professor

Accepted by   Joseph Paradiso

Academic Head, Program in Media Arts and Sciences

Piezoelectric single crystal based one-dimensional phased array for breast tissue imaging

by

Wenya Du

Submitted to the Program in Media Arts and Sciences, School of Architecture and Planning, on

August 15, 2024, in partial fulfillment of the requirements for the degree of

Master of Science

Abstract

Ultrasound is widely used in clinical practice because it is safe, non-invasive, non-ionizing, low-cost, and provides real-time imaging, monitoring, and therapy. However, conventional ultrasound probes are rigid, pressure-required, and operator-dependent. Replacing rigid transducers with conformable ultrasound transducer arrays can allow image acquisition on curved body parts, improve image quality, and enable functions such as long-term monitoring. In this thesis, I propose a conformable ultrasound breast patch (cUSBr-Patch) consisting of a one-dimensional (1D) phased array and a nature-inspired patch design, which offers large-area, deep tissue scanning and multi-angle, repeatable breast imaging while avoiding the drawbacks of conventional ultrasound imaging technologies. I used a Yb/Bi-doped PIN-PMN-PT single crystal as the active element due to its superior piezoelectric properties (d_{33} = 2,800 pC/N, ε_r = 7,000, k_{33} = 0.93). I then fabricated a 1D phased array transducer consisting of 64 elements with an operational frequency of 7.0 MHz. The 1D array exhibits promising acoustic performance with i) a maximum imaging depth of 80 mm, ii) contrast sensitivity of 3 dB, iii) axial/lateral resolutions of 0.25/1.0 mm at 30 mm depth, and iv) a larger field of view than the commercial handheld linear probe at depths of approximately 30 mm or deeper, indicating a potential reliable capability to detect early-stage breast tumors. Beyond this, comprehensive *in vitro* experimental studies establish that the cUSBr-Patch can provide accurate and reproducible imaging of different phantoms. The clinical trials reveal that the patch exhibits a sufficient contrast resolution (~3 dB) and axial/lateral resolutions of 0.25/1.0 mm at 30 mm depth, allowing the observation of small cysts (~ 0.3 cm) in the breast. This research develops a first-of-its-kind ultrasound technology for breast tissue scanning and imaging which offers a non-invasive method for tracking real-time dynamic changes of soft tissue.

Thesis advisor: Canan Dagdeviren

Title: Associate Professor in Media Arts and Sciences

Piezoelectric single crystal based one-dimensional phased array for breast tissue imaging

by

Wenya Du

The following people served as readers for this thesis:

Thesis Advisor: _____

Canan Dagdeviren, Ph.D.

Associate Professor

Media Arts and Sciences, Media Lab

Thesis Reader: _____

Robert Langer, Ph.D.

David H. Koch Institute Professor

Department of Chemical Engineering

Thesis Reader: _____

Hugh Herr, Ph.D.

Professor

Media Arts and Sciences, Media Lab

Acknowledgments

Finally, I deeply thank Tod Machover, Joseph Paradiso, and Mahnaz El-Kouedi for their support during my study at MIT Media Lab. In addition, I extend my deepest gratitude to my lovely family—my husband, my son Noah, my mother, mother-in-law, and father-in-law—for their unwavering support and affection in all of my endeavors, academic and otherwise. This present is intended for my daughter Aria, who was born while I was pursuing this master's degree.

Table of Contents

List of Figures

List of Tables

Chapter 1 Background and Research Motivation

1.1   Conformable electronics for healthcare and biomedical applications

1.1.1   Recent development of conformable electronics

In recent decades, healthcare and medical systems have encountered significant difficulties, primarily due to the escalating health demands of society and unpredictable health issues that have emerged globally [1]. An increasing number of individuals are recognizing that the majority of non-communicable diseases stem from a lack of physical activity, inadequate nutrition, and unhealthy lifestyle choices. The systematic gathering and immediate analysis of physiological vital signs have become crucial in protecting individuals from the emergence and advancement of illnesses in contemporary society. Conventional centralized healthcare services necessitate individuals to personally visit hospitals to receive medical treatment, which can result in delays in meeting their healthcare requirements. However, it is crucial to recognize that the wide array of inflexible instruments and diagnostic methods have several drawbacks, such as inadequate compatibility with living organisms, dependence on highly skilled individuals, and unpleasant patient encounters [2]. There is a strong demand for medical equipment or systems that enable patients to independently monitor and manage their own health issues. Conformable electronics have gained considerable attention in recent years and are poised to revolutionize conventional healthcare monitoring and diagnosis. This is achieved by integrating features such as portability, wearability, remote access, and timely data collection [3, 4]. A variety of flexible electronics with different substrates and matrices (i.e., polymers [5], elastomers [6], textiles [7], aerogels [8], hydrogels [9]) — have been demonstrated for monitoring a wide range of health-relevant parameters — such as electrophysiological (e.g., electrocardiogram (ECG), electroencephalogram

(EEG), electromyography (EMG), electrooculogram (EOG))[10], physiological (e.g., blood pressure [11], pulse [12], temperature [13]), thermal (e.g., thermal conductivity, temperature distribution[14]), mechanical [15, 16] (e.g., strain [17], pressure [18, 19]) and biochemical information (e.g., glucose/lactate [20], hydration [21], pH [22, 23], sweat [24], local field potential [25]), have continuously emanated from the human body.

Piezoelectric materials, which serve as intelligent materials connecting electrical and mechanical energy, have been widely employed in various electronic devices in recent years. Advancements in mechanical engineering and material fabrication technology have enabled the creation of high-performance piezoelectric devices that can be shaped to fit various forms. These devices show great potential for use in bio-integrated applications [15, 16, 26-28]. Piezoelectric conformable electronics, fabricated from ceramics, crystals, composites [8, 29, 30], thin film, polymers, fibers [31], have demonstrated real-time and continuous signal monitoring and decoding for diverse soft tissue biomedical and healthcare applications, ranging from sensing [32, 33] to energy harvesting [15, 34-36] and human-machine interactions [37], including in understanding body motion, facial motion [6, 38], skin modulus [17, 39], heart motion [40, 41], gastrointestinal motility [5], tactile stimuli [42], blood pressure [19, 43], and blood flow [44]. Nevertheless, the majority of these devices focused primarily on physiological signals obtained from the external surface of the human body or the surface of tissues and organs, providing only limited insights into the internal structures of deep tissues and organs. Deciphering information from deep tissue, which is essential for understanding the complex mechanisms underlying various diseases, is highly intriguing.

1.1.2   Conformable ultrasound electronics

Ultrasound technology, a highly utilized and rapidly advancing method for diagnosis and treatment, has been extensively studied for its application in deep tissue medical diagnosis. It offers several benefits compared to magnetic resonance imaging (MRI), which does not provide real-time imaging and is costly, as well as computed tomography (CT), which involves ionizing radiation and poses risks. Ultrasonic waves are commonly generated through various physical phenomena, including magnetostrictive, electrostatic, electrodynamic, piezoelectric, and capacitive effects [45]. The piezoelectric effect is the most common operating principle for actuating and sensing ultrasonic signals [46, 47]. The ultrasonic method is highly suitable for non-destructive testing (NDT), biomedical, and healthcare applications due to its distinctive features, including exceptional precision, strong ability to penetrate deep tissues, remarkable sensitivity, and non-ionizing radiation. In recent decades, there has been extensive research on the design principle, materials, configurations, fabrication, and applications of traditional ultrasound transducers [46, 47]. Although ultrasound technologies have numerous benefits, conventional ultrasound probes are bulky and hard. Additionally, an operator must maintain a stable grip on the probes to ensure a reliable acoustic coupling interface, a sufficient field of view, and the desired penetration direction. Currently, ultrasound probes are unable to fully encompass the curved surfaces of certain body parts, such as the elbow, skull, knee, or larger areas like the breast, abdomen, or fetus [48].
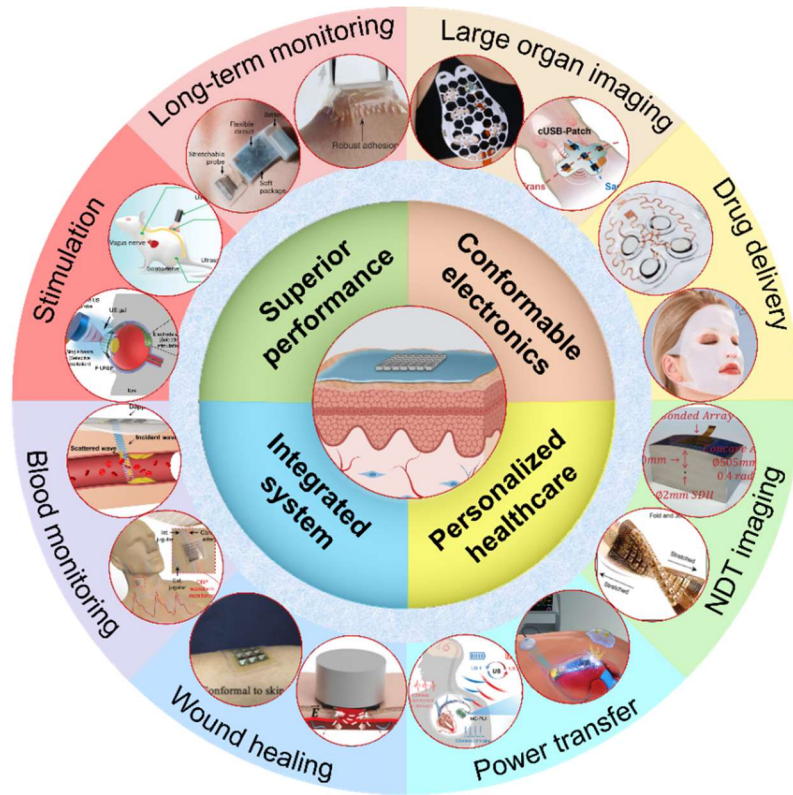
Figure 1.1. Overview of the most current advancements and innovations in conformable ultrasound electronics (cUSE). The conformable electronics with the integrated data acquisition system exhibit superior ultrasound performance for non-destructive testing and biomedical applications [55-70].

Hence, there is a significant demand for mechanically deformed ultrasonic transducers that can adhere to the skin without any issues and still maintain their ultrasound functionality. These transducers are crucial for achieving accurate imaging, long-term monitoring, precise therapy, and various other applications [49]. The concept of conformable ultrasound electronics (cUSE) was initially proposed prior to 2010 [48, 50] and has since been extensively studied over the past six years [51-55]. This research has not only addressed existing constraints of inflexible and cumbersome ultrasound probes but has also advanced the field of conformable electronics for healthcare through the development of diverse designs and technologies. Several fabrication strategies have been used to propose and create numerous cUSE for healthcare monitoring and

biomedical applications in recent studies (**Figure 1.1**), including stretchable [56] and bendable [57] devices imaging on complex surfaces, long-term monitoring with bio-adhesion [58] or integrated system [59], large organ monitoring (breast tissue [60], bladder volume [61]), cardiac monitoring [62], blood pressure monitoring [43], blood flow monitoring [44], energy harvesting [63], power transfer for implant device [64], tissue repair [65], chronic wound healing [66], retinal stimulating [67], peripheral nerve stimulation [68], brain stimulation [69], drug delivery on faces [70], transdermal cosmeceutical delivery [71], and several other biomedical applications. Despite recent proposals for wearable and flexible piezoelectric ultrasound devices, there are still unexplored research opportunities in this field. These include incorporating cutting-edge piezoelectric materials with ultrasound technologies and achieving standardized and reliable scanning of large-area curvilinear soft tissues without applying transducer compression, in order to enable accurate image reconstruction.

1.2   The detection target: breast tissue and tumor

Breast cancer is the predominant form of cancer among women globally, with approximately 2.26 million new cases reported in 2020 [72]. Nevertheless, there has been a consistent decrease in mortality rates attributed to breast cancer as a result of advancements in treatment methods and the implementation of screening technologies for early detection. Timely identification of breast cancer is crucial for both survival and the prevention of disease development. Since 1989, mortality rates have exhibited a downward trend as a result of improved early detection through screening, heightened awareness, and the utilization of advanced treatment methods [73]. The statistics report emphasized the utmost importance of early detection and treatment of breast cancer, highlighting the significance of regular screening for all women, regardless of the stage of the disease [74]. Breast imaging plays a crucial role in the detection and management of breast cancer.

These technologies have the capability to detect cancer at an earlier stage, before it becomes noticeable through touch, thereby enabling earlier intervention and care. Nevertheless, numerous obstacles exist at the international level that impede women from attaining access to fundamental services. The barriers encompass financial constraints, limited access to advanced technology for early breast cancer detection, and efficacy concerns, particularly in developing nations [75]. This section provides a brief summary of the background information on breast tissue and tumors, as well as an overview of the current ultrasound technologies used for breast examination.

1.2.1 Early-stage breast cancer

The TNM method, established by the American Joint Committee on Cancer (AJCC), is the prevailing staging system for breast cancer [76, 77]. The abbreviations T, N, and M denote the tumor's extent (size) (T), metastasis to distant sites (M), and lymph node metastasis (N), respectively. Stages of breast cancer are conventionally delineated using numerical values between 0 and IV. Stage 0 signifies non-invasive cancers that have not metastasized beyond the breast and have metastasized to other anatomical sites.

Early-stage breast cancer is characterized by a tumor size of less than 5 centimeters and has not met the criteria for metastasis beyond the breast or axillary lymph nodes. It consists of ductal carcinoma in situ (DCIS) as well as breast malignancies in stages I, IIA, and IIB [78, 79]. DCIS and other non-invasive breast lesions are categorized as stage 0. In stage 0, there is an absence of indications of cancer cells or non-cancerous aberrant cells escaping from the site of origin in the breast, infiltrating adjacent normal tissue, penetrating it, or passing through it. Invasive breast cancer is characterized by its ability to penetrate or infiltrate healthy surroundings of breast tissue, constituting stage I. In Stage I, the subcategories IA and IB are distinguished. Stage IA breast cancer is generally classified as invasive when the tumor has not met the criteria of a 2 cm diameter,

lacks metastasis beyond the breast, and does not impact lymph nodes. Stage IB generally denotes invasive breast cancer characterized by the presence of minuscule clusters of cancer cells in lymph nodes, measuring greater than 0.2 mm but less than 2 mm in diameter. Stage II is further classified into two subcategories, namely IIA and IIB, which delineate lesions ranging in size from 2 cm to 5 cm.

1.2.2 Breast quadrants

There are fifteen to twenty lobes of glandular tissue in the breast, which are divided into connective tissue and adipose tissue. Open lactiferous ducts transfer secreted milk to the nipple from the lobes. A correlation exists between breast density and the density of glandular tissue and the ductal system. In comparison to women with lesser breast density, those with greater breast density are believed to have an increased cancer risk. In addition, it is critical to utilize breast quadrants to comprehend and standardize the reporting of tumor location and to collect additional information regarding the tumor. Perpendicular lines intersecting at the nipple can be used to divide each breast into four quadrants: Upper-Outer (UOQ) representing superolateral; Upper-Inner (UIQ) representing superomedial; Lower-Outer (LOQ) representing inferolateral; and Lower-Inner (LIQ) representing inferomedial (**Figure 1.2**). Each quadrant possesses unique characteristics and offers supplementary prognostic data pertaining to breast cancer [80]. Most breast parenchyma is located in the upper peripheral quadrant. As a result, benign and malignant breast pathologies prevalently manifest in the upper-outer breast quadrant. Nonetheless, fatality rates for tumors located in the upper-outer breast quadrants are comparatively lower. The occurrence of malignancies is least frequent in the lower inner quadrant. Medial breast and inner quadrant tumors are associated with higher mortality rates. This could be attributed to the challenge

of mammography detection in the interior quadrants and the advanced stage of the cancer at the time of diagnosis [81].
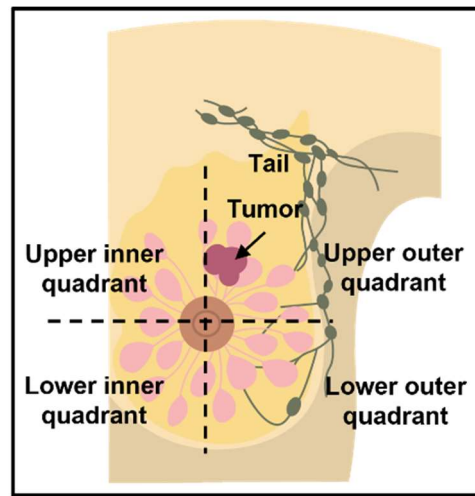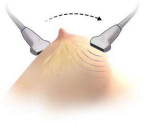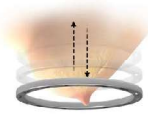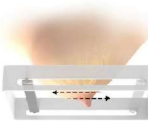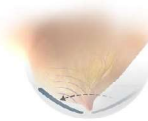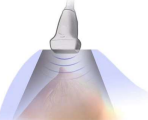
Figure 1.2. The schematic of the breast quadrants.

1.3   Current ultrasound technologies for breast examination

Among the numerous imaging modalities are mammography, ultrasound, and MRI. Mammographic screening has been empirically demonstrated to reduce mortality through early detection [82, 83]. Notwithstanding this, mammographic sensitivity in dense breasts may be significantly diminished, falling below 50% [84]. Consequently, and in light of the confirmation that breast density is an autonomous risk factor for breast cancer, there is an increasing need for an additional instrument. As a diagnostic adjunct to mammographic imaging, ultrasound is frequently employed when the latter remains the gold standard for breast cancer. In cases where an abnormality is identified through a physical examination or a mammogram, the most effective method to distinguish between fluid-filled and rigid irregularities (e.g., benign cyst or benign fibroadenoma) is to conduct an ultrasound test [82]. Typically, a breast ultrasound is performed to

determine whether a mammogram or tactile examination of the breast has detected a fluid-filled cyst or a solid tumor.

Table 1.1. The summary of current breast image methods and commercially available breast imaging products

Methods	Schematic	Company products	Working principle	Patient's posture	Pressure on breast	Frequency range
Handheld		• Hologic Viera • Echonous • Eagleview	Scan at different areas by the operator	Any	Yes	6-15 MHz
Ring array		• Delphinus SoftVue • Lily MedTech	The ring array moves in the vertical direction	Prone (water bath)	No	5-10 MHz
Flat plate		• GE Invenia • Siemens Acuson • CapeRay Aceso	Linear/curved array scans long horizontal direction	Supine	Yes	6-15 MHz
Bowl shape		• Hitachi SOFIA	Linear array rotates circular 360º	Prone (water bath)	No	5-10 MHz
3D scan		• Isono Health	A bulky probe inserts into a bra holder and then rotates circularly	Any	No	5-10 MHz

As an additional screening method, handheld ultrasonography (HHUS) is a viable option due to its affordability and widespread availability. HHUS was investigated in multiple studies as a potential screening method for women with dense breast tissue [85]. However, there are some limitations to HHUS screening, including a high incidence of false positives (FP) and a substantial time investment on the part of the physician for exam execution and interpretation [86]. As a consequence of these limitations, years have been devoted to technological research in an effort to

develop ultrasound instruments that can standardize and streamline examinations in the United States. The objective of developing automated breast ultrasound (ABUS), which differs depending on the manufacturer, was to eliminate the operator-dependent nature of HHUS and increase the examination's reproducibility. ABUS is a technological innovation that facilitates the visualization of breast tissue in three dimensions via ultrasound. It offers the additional advantages of multiplanar reformations and the ability to review images retrospectively subsequent to the examination [87].

In conclusion, the human breast poses a unique challenge in terms of deep tissue imaging over a large area, due to the fact that its geometry and deformability vary considerably not only between subjects but also over time and age within a single subject. Ultrasound therefore assumes a critical position in the diagnosis and treatment of breast cancer due to its capability of extracting meaningful images from diverse presentations of breast tissue [88, 89]. Present ultrasound breast imaging technologies, HHUS and ABUS, are preferred methods (**Table 1.1**). However, there are still technical challenges that must be addressed before ultrasound can be considered a dependable option for breast screening. These challenges include the following: (i) HHUS manual scanning of the entire breast through strong compression requires the technician to possess the necessary expertise and training; and (ii) ABUS can scan the entire breast simultaneously; however, inadequate skin contact persists due to the use of a liquid medium. Addressing these deficiencies could not only facilitate physicians in evaluating breast imaging with greater dependability, but also offer an approach to early detection of breast anomalies that is accessible, economical, and easy to use. Clearly, a conformable patch that demonstrates improved acoustic properties, dependable imaging capability, and seamless operation while capturing a complete image of the typical four quadrants of the breast is extremely favorable in terms of both transducer performance

(e.g., superior material properties) and breast imaging (e.g., repeatability of array position, absence of applied compression, etc.).

1.4   Objective and outline of this thesis work

1.4.1   Objective and Achievement

In this work [60], collaborating with others students, researchers and doctors, I worked with team members developed a conformable ultrasound breast patch (cUSBr-Patch) that circumvents the limitations of conventional ultrasound imaging technologies. It is comprised of a one-dimensional (1D) phased array and an intuitively operable patch design inspired by nature. This patch enables deep tissue scanning over a wide area and permits repeatable breast imaging from multiple angles. A 1D phased array transducer was constructed me, comprising 64 elements, operating at a frequency of 7.0 MHz. The 1D array demonstrates encouraging acoustic characteristics, including i) an imaging depth of no less than 80 mm, ii) a contrast sensitivity of 3 dB, iii) axial and lateral resolutions of 0.25 and 1.0 mm, respectively, at a depth of 30 mm, and iv) a field of view that surpasses that of the commercial handheld linear probe at depths of 30 mm or more. These results suggest that the 1D array has the potential to reliably detect breast tumors in their early stages. In addition to this, extensive in vitro experimental investigations demonstrate that the cUSBr-Patch is capable of delivering precise and consistent imaging across various phantoms. By incorporating 360-degree rotation capabilities at each position and a scanning trace to physically guide transducer positioning into a honeycomb patch inspired by nature, the 1D array is capable of covering the entire breast surface and reconstructing multi-angle images from various views. As a result, imaging artifacts caused by inadequate positioning capabilities, which are fundamental issues that plague current ultrasound technologies for whole-breast or large-area

screening, are eliminated. This study introduces a groundbreaking on-body ultrasound technique for imaging and screening breast tissue. It also provides an innovative, non-invasive method for monitoring the dynamic changes that occur in breast tissue.
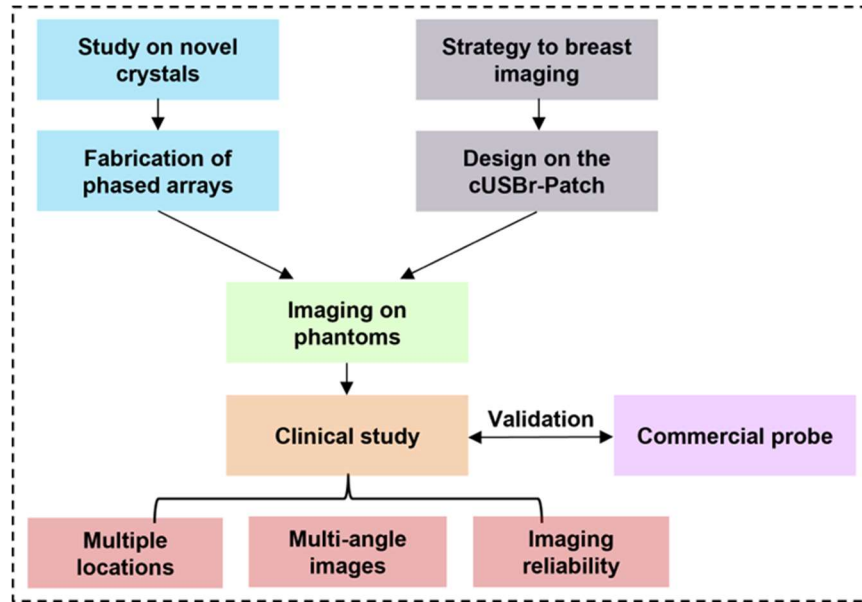
Figure 1.3 The research flow of this study.

The research flow shown in **Figure 1.3** illustrates the novelty and structure of this work. The PI (Prof. Canan Dagdeviren) designed the research direction and directed all technical research activities. Dr. Dabin Lin from Xi'an Technological University processed and characterized the piezoelectric crystals, and then provided the crystal for device fabrication. Under the supervision of Dr. Lin Zhang, I designed, fabricated, and characterized the 1D phased array. Emma Suh and Avani Ahuja designed and fabricated the patch with my assistant. I worked with Colin Marcus and Dr. Lin Zhang and conducted the imaging on phantoms. Colin Marcus operated the Vantage 256 system and conducted all image processing. Lara Ozkan helped me with the imaging scripts and Institutional Review Board (IRB) documents. I worked with the PI to execute the *in vivo* study for breast tissue imaging.

1.4.2 Outline of my thesis

In this thesis, I will first give the background of piezoelectric ultrasound transducer, then mainly focus on the design, fabrication, and performance of the 1D array, imaging on phantoms, and the clinical study. Additional accomplishments and research details, including the honeycomb patch design and fabrication, processing and characterization of the single crystal, image acquisition, and illustration, are detailed in our most recent publication in Science Advances [60].

Chapter 2 briefly introduces the background of piezoelectrics, piezoelectric materials, and the fundamentals of ultrasonic transducers. I will mainly focus on the critical parameters of piezoelectric materials and design structures of transducers.

Chapter 3 illustrates how to design, fabricate, and characterize a single crystal based 1D phased array transducer. In this chapter, I will show the simulation of the electrical and acoustic properties of the manufactured transducer using KLM (Krimholtz, Leedom, and Matthaei) models, and will also address the essential criteria that must be met when designing matching and supporting layers for specific single crystal and related working frequency. The detailed methodologies of micromachining and microfabrication are shown step by step. In addition, the characterization of transducers, the determination of working frequency and bandwidth, and the acoustic performance of the phantoms are also described.

Chapter 4 mainly focuses on the procedure of the clinical study and the ultrasound imaging on the breast tissue. We first imaged the subject's breasts using the cUSBr-Patch with the Vantage 256 system and then cross-validated the results by an ML6-15 linear probe with the GE Logiq E10 system. The imaging performance stability and multiangle image reconstruction are also illustrated.

Chapter 5 summarizes the results of this work and discusses future research suggestions.

Chapter 2   Fundamentals of ultrasound transducer

2.1.   Piezoelectrics and materials

2.1.1. Piezoelectricity

Piezoelectricity is a unique property of certain non-centrally symmetric crystalline materials[90]. The piezoelectric effect is a reversible phenomenon that manifests in two ways: firstly, when mechanical stress is applied, it induces electric polarization; and secondly, when an electric field is applied, it induces mechanical strain. These two effects are crucial for numerous electronic devices, such as transducers, actuators, and sensors (**Figure 2.1**) [47, 91-94]. The piezoelectric coefficient for each material has its own value with respect to its crystal orientation [90]. Polarization of a suitable material through the application of an adequate electric field is necessary to induce piezoelectric properties. It is common practice to subscribe or describe piezoelectric properties with two numbers. The initial subscript denotes the direction in which the applied electric field or generated charge is oriented. The direction denoting the strain or mechanical tension is specified by the second subscript.

While piezoelectric materials can exhibit a diverse array of properties and piezoelectric coefficients, their selection is contingent upon the desired mode of vibration. In the context of a vibrational mode, the role of thickness is of considerable importance. In situations where thickness or out-of-plane vibration monitoring are necessary, a piezoelectric element characterized by a greater d_{33} property is selected.
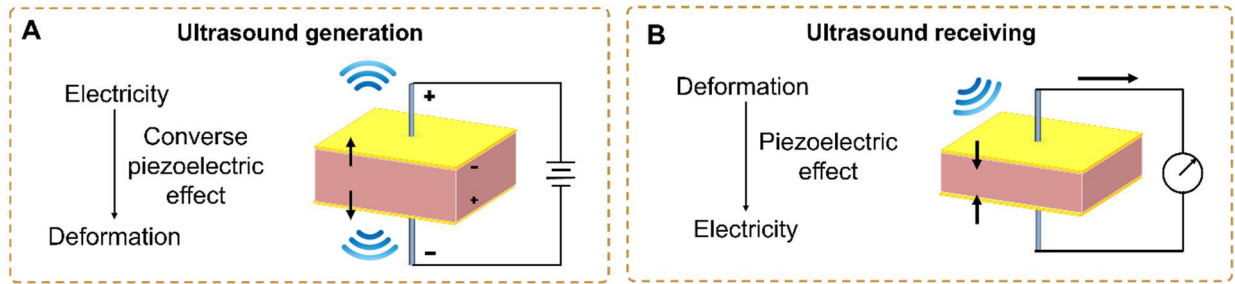
Figure 2.1 The working principle of piezoelectrics for ultrasound. A) Ultrasonic generation based on the converse piezoelectric effect. B) Ultrasonic receiving based on direct piezoelectric effect.

2.1.2. Critical parameters of piezoelectric materials

Numerous parameters must be established within the domain of materials science to characterize the attributes of piezoelectric materials. When formulating an ultrasonic transducer, the four material properties that hold the utmost significance are dielectric, piezoelectric, electromechanical, and acoustic characteristics, including the piezoelectric coefficient (d_{33}), dielectric permittivity (ε_r), electromechanical coupling coefficient (k), and acoustic impedance (Z). Furthermore, considerable attention has been devoted to the application of piezoelectric composites on account of their improved electromechanical coupling, which can facilitate energy transmission and assist in the expansion of bandwidths, thereby substantially enhancing the signal-to-noise ratio (SNR). The electrical impedance of ultrasound transducers is subject to variation due to changes in dielectric permittivity, which are influenced by temperature and electric field.

The electrical port associated with an ultrasonic transducer is a capacitor structure, which is the dielectric between two parallel electrodes, due to the fact that the piezoelectric material is a capacitor [95, 96] A dielectric is an electrical insulator that can respond to external electric stimulation.[97] When an AC electric field is applied to the dielectric material, the dielectric

permittivity (ε^*) shows a complex form [98]. The dielectric loss (tanδ) is the phase difference between D and E. It represents the transformation of a fraction of the electric energy into thermal energy in the presence of an external electric field. Ascertaining the clamped capacitance of an ultrasonic transducer requires knowledge of the area, thickness, and clamped dielectric permittivity of the piezoelectric material. Furthermore, dielectric permittivity is an essential parameter for matching the transducer's electrical impedance with that of the driving electronics. In order to optimize power transfer, it is imperative that the input electrical impedance of the ultrasonic transducer is tangible at the desired frequency, and that its input resistance is equivalent to the electrical impedance of the source, which is generally set at 50 Ω in termination.

An essential parameter for determining the capacity of piezoelectric materials to convert energy between electrical and mechanical forms is the electromechanical coupling factor. It is not a constant material property; rather, it is contingent on the material's geometry. For instance, a material's k coefficient is higher in a rod shape than it is in a plate form [90]. When designing a transducer, a high k value is favored due to its ability to enhance energy conversion, expand bandwidth, and improve sensitivity. An estimation of the coupling factor can be achieved by utilizing the measured resonance and anti-resonance frequencies of a piezoelectric element, contingent upon the vibration mode in which the element is excited. The internal speed of sound of a substance governs both its resonant frequency and acoustic impedance; this is an intrinsic property of the substance. As stated previously, impedance matching between the transducer and the medium of propagation is critical for optimizing the performance of the transducer. Along with other critical parameters and equations of piezoelectric materials, the most prevalent coupling variables for vibration in a circular disk along the radial and thickness axes are typically denoted as k_{33} or k_p and k_t. These variables are described and summarized in **Table 2.1**. Further optimization

of the transducer's performance can be achieved by modifying the configuration of the piezoelectric element and selecting the appropriate piezoelectric material for a given transducer [47]. Generally, a compromise on other characteristics is required due to the fact that the majority of applications require a combination of qualities [99].

Table 2.1 Critical parameters and equations of piezoelectric materials

Properties	Symbol	Name	Equation	Notes
Piezoelectric properties	s^E	Compliance under a constant electrical field	$\begin{bmatrix} S \\ D \end{bmatrix} = \begin{bmatrix} s^E & d \\ d & \varepsilon^T \end{bmatrix} \begin{bmatrix} T \\ E \end{bmatrix}$	Direct/converse piezoelectric effect
	ε^T	Dielectric permittivity under a constant stress		
	d_{ij}	Piezoelectric coefficient	$d_{ij} = k_{ij} \cdot \sqrt{s^E \cdot \varepsilon^T}$	d_{33} can be directly measured by the d_{33} meter.
	g_{ij}	piezoelectric voltage coefficient	$g_{ij} = d_{ij}/\varepsilon^T$	-
	d_h	Hydrostatic piezoelectric charge coefficient	$d_h = d_{31} + d_{32} + d_{33}$	-
Dielectric properties	$\varepsilon_{ij}, \varepsilon_r,$	Dielectric permittivity	$D_{ij} = \varepsilon_{ij} \cdot E_j, C = \frac{\varepsilon_0 \varepsilon_r A}{d}$	D is the electrical displacement
	$tan\delta$	Dielectric loss	$\tan \delta = \frac{\varepsilon_r''}{\varepsilon_r'}, \varepsilon_r^* = \frac{\varepsilon^*}{\varepsilon_0} = \varepsilon_r' - j\varepsilon_r''$	-
	Z	Electrical impedance	$Z \propto \frac{1}{j\omega C} = \frac{t}{j2\pi A\varepsilon_r'}$	Transducer's input Z must equal the source's Z.
	E_c	Coercive field	-	A large coercive field is critical for high-power transducers
Electro-mechanical properties	k	Electromechanical coefficient	$k^2 = \frac{converted\ mechanical\ energy}{input\ electric\ energy} = \frac{converted\ electric\ energy}{input\ mechanical\ energy}$	
	k_p	electromechanical coupling factors	$k_p^2 = \frac{1}{p}\frac{f_a^2 - f_r^2}{f_a^2}$	Thin disk-shape samples
	k_t	electromechanical coupling factors	$k_t^2 = \frac{\pi}{2}\frac{f_r}{f_a} \cot\left(\frac{\pi}{2}\frac{f_r}{f_a}\right)$	Thin disk-shape samples
	k_{33}	electromechanical coupling factors	$k_{33}^2 = \frac{\pi}{2}\frac{f_r}{f_a} \cot\left(\frac{\pi}{2}\frac{f_r}{f_a}\right)$	Longitudinal mode
	k_{31}	electromechanical coupling factors	$\frac{k_{31}^2}{k_{31}^2-1} = \frac{\pi}{2}\frac{f_a}{f_r} \cot\left(\frac{\pi}{2}\frac{f_a}{f_r}\right)$	Transverse mode
	Q_m	Mechanical quality factor	$Q_m = \frac{f_r}{\Delta f}$	Δf is at -3 dB of the maximum admittance.
Acoustic properties	v_{33}	longitudinal acoustic velocity	$v_{33} = 2f_a \cdot t$	t is controlling dimension of the piezoelectric element (thickness)
	Z_p	Acoustic impedance	$Z_p = \rho \cdot v_{33}$	ρ is the density of the sample
	N	Frequency constant	$N = f_a \cdot t$	f_a is the anti-resonance frequency.
Temperature	T_c	Curie temperature	$\varepsilon = \frac{C}{T - T_C}$	C is the Curie-Weiss constant. A greater T_c can guarantee transducer a wider temperature operating range.

2.1.3. Lead based piezoelectric ceramics and single crystals

Piezoelectric lead zirconate titanate [Pb(Zr$_{1-x}$Ti$_x$)O$_3$] ceramics, specifically PZT, are commonly employed as the active components in ultrasound probes due to their cost-effectiveness and reliable piezoelectric properties. These ceramics exhibit well-developed and stable

characteristics (d_{33} < 700 pC/N, k_{33} < 0.7), particularly when their compositions are close to the morphotropic phase boundary (MPB) [100]. The majority of conformable ultrasound devices use commercial PZT [43, 44, 56, 62, 101-106]. MPB compositions exhibit unusually high dielectric and piezoelectric properties due to their increased polarizability resulting from the interaction between two equivalent energy states, specifically the tetragonal and rhombohedral phases [107]. This enables the optimal domain reorientation during the poling process. Researchers not only studied PZT, but also explored a diverse range of piezoelectric compositions in order to make additional modifications using acceptor and donor dopants [108]. Several complex lead-based relaxor materials $Pb(B'B'')O_3$ and $Pb(B'B'')O_3 - PbTiO_3$ ($B' = Mg^{2+}, Zn^{2+}, In^{3+}, Ni^{2+} \cdots$, $B'' = Nb^{5+}, Ta^{5+}, W^{6+} \cdots$) have been intensively studied,[109] among them, PMN-PT and $PbMg_{1/3}Nb_{2/3}O_3$-$PbTiO_3$ (PMN-PT), $PbZn_{1/3}Nb_{2/3}O_3$-$PbTiO_3$ (PZN-PT) and xPb(In$_{1/2}$Nb$_{1/2}$)O$_3$– yPb(Mg$_{1/3}$Nb$_{2/3}$)O3–zPbTiO3 materials are most attractive ceramics due to their exceptional piezoelectric performance [110]. Furthermore, traditional piezoceramics, characterized by grain sizes ranging from 5 to 10 micrometers, are not optimal for high frequency transducer applications due to the active components' dimensions potentially reaching tens of micrometers. PMN-PT ceramics, known for their high clamped dielectric permittivity, are currently being produced in tiny grain forms. This is crucial for the high frequency transducer and dicing operations [111] In addition, Zhang's and Li's research teams effectively tackled the persistent obstacle of synthesizing novel piezoelectric ceramics by incorporating dopants into the localized structural heterogeneity of a particular ferroelectric system. As a result, they achieved unprecedented levels of dielectric and piezoelectric properties in the newly developed ceramics [112, 113]. After that, rare-earth (RE) single doped or co-doped element (RE = La^{3+}, Sm^{3+}, Pr^{3+}, Yb^{3+}, Eu^{3+}) doped or co-doped PMN-PT and PZN-PT ceramics have attracted the interest of researchers due to their ultrahigh d_{33} and

k_{33}. Very recently, RE-doped PMN-PT and RE-doped PIN-PMN-PT based transducers have been developed for piezoelectric transducer design [114, 115], which achieved enhanced acoustic performance for imaging.

In recent years, single crystal relaxors have gained interest due to their advantages over PZT systems [116, 117], such as simpler crystal formation around MPB compositions and superior piezoelectric and electromechanical capabilities achieved through domain engineering [90, 118, 119]. For example, due to improved polarizability brought on by the connection between two equivalent energy levels, PMN-PT single crystals possess very good piezoelectric characteristics ($k_{33} > 85\%$ and $d_{33} =$ 1,200 ~ 2,500 pC/N). Moreover, the utilization of domain engineering techniques, which include the modification and alignment of crystal domains in directions different from the spontaneous polarization direction of single crystals, has greatly contributed to improving their electrical properties [90]. Studies have demonstrated that PMN-PT single crystal transducers outperform PZT transducers in terms of acoustic performance in both large transducers with single elements and phased arrays. These advantages include wider bandwidth, shorter pulse length, and enhanced axial and lateral resolutions [47, 120, 121]. However, the Curie temperature T_c (~150 ºC) and rhombohedral to tetragonal phase transition temperature $T_{r\text{-}t}$ (70-90 ºC) are quite low for PMN-PT solid solutions [118]. It is widely acknowledged that thermal stability and outstanding electromechanical performance cannot be achieved simultaneously. Therefore, it is essential to discover alternative solutions to the limitations of piezoelectric materials [90, 108]. Furthermore, in many electromechanical applications, particularly those that involve powerful transducers and actuators operating in high magnetic fields, the combination of a robust piezoelectric response and a significant coercive field (E_C) enables improved operational efficiency and a broad range of functional capabilities. Hence, the quest for innovative relaxor-PT systems that meet the following

characteristics presents an urgent undertaking: i) high critical temperature and transition temperature, ii) high piezoelectric coefficient, or iii) large coercive field [122-125]. Researchers have discovered that PIN-PMN-PT single crystals, which are close to the MPB composition, exhibit a high T_c of 200 ºC and demonstrate piezoelectric performance that is similar to that of PMN-PT single crystals. Ternary single crystals have become increasingly popular for ultrasound transducer applications. The addition of rare earth elements as dopants can boost both thermal stability and piezoelectric properties, similar to ceramics.

2.2. Ultrasound transducers

2.2.1. Structure and parameters of transducers

Three-port network. The central element of the ultrasound system is the ultrasound transducer. The efficacy of the ultrasound transducer is primarily dictated by its design. While the design of a transducer may vary significantly to accommodate different requirements, the fundamental components remain the same. Medical ultrasound diagnostics utilizes two main types of ultrasonic transducers: single-element and array transducers, which encompass linear array and phased array. Images are produced by single-element transducers using mechanical scanning. On the other hand, clinical ultrasound imaging systems tend to choose array transducers that employ electronic scanning due to their multitude of advantages. These include the capacity to capture images at a high frame rate, the capability to dynamically focus, the ability to quantify flow in real-time, and the simplicity they offer in a clinical setting. An ultrasound transducer is generally considered as a three-port network (**Figure 2.2 A**), consisting of two acoustic ports located on the front (matching layer) and back (backing layer) sides of the piezoelectric material, and one electrical port that is connected to the driving/receiving circuits [47]. The primary structural components, arranged from

bottom to top, include the backing layer, active layer, matching layer, and optional focusing lens. To ensure electrical shielding and safety, the transducer is enclosed in grounded housing.

Matching layer. Piezoelectric materials possess an acoustic impedance of 30 MRayl, which is significantly more than the acoustic impedance of biological tissues (1.5 MRayl). Ultrasound waves are reflected at the interface due to the mismatch in acoustic impedance, resulting in their inability to efficiently propagate over the interface. Hence, the inclusion of an acoustic matching layer is crucial as it enhances the sensitivity, bandwidth, and energy transfer efficiency of the transducer. To achieve optimal matching performance, the design of the matching layer necessitates precise control over both the acoustic impedance and thickness. The acoustic impedance of the matching material is adjusted by combining high impedance particles (such as metal particles or metal oxide particles) with low impedance polymer (such as Epoxy) in a specific proportion [47].

Backing layer. When an electrical source stimulates a transducer, it vibrates at its inherent resonance frequency. In continuous-wave applications, the transducers are air-backed to optimize the forward radiation of energy. As a result of the difference in acoustic impedance between air and piezoelectric material, sound energy is reflected in the forward direction at this boundary [126]. Consequently, an insignificant quantity of energy is dissipated via the back port. This discrepancy, which produces the aforementioned ringing effect in pulse-echo applications, is highly undesired since it leads to an increase in the duration of the pulse. In order to minimize the occurrence of ringing or increase the range of frequencies, it is possible to use absorbent backing materials that have similar acoustic impedances to the piezoelectric material. The purpose of the backing material is to minimize the discrepancy in acoustic impedance and also to attenuate a portion of the energy generated by the vibration of the rear face. The energy that enters it is fully absorbed. It is important

to note that in order to suppress ringing or reduce pulse duration, sensitivity must be compromised due to the absorption of a considerable amount of energy by the supporting material [127]. As a result, sensitivity and pulse duration are usually traded off to increase a transducer's sensitivity by altering the backing layer impedance. Tungsten-loaded epoxy and Esolder 3022 are quite popular for backing material, and the impedance can range from 8 to 20 MRayl [46, 47, 128].
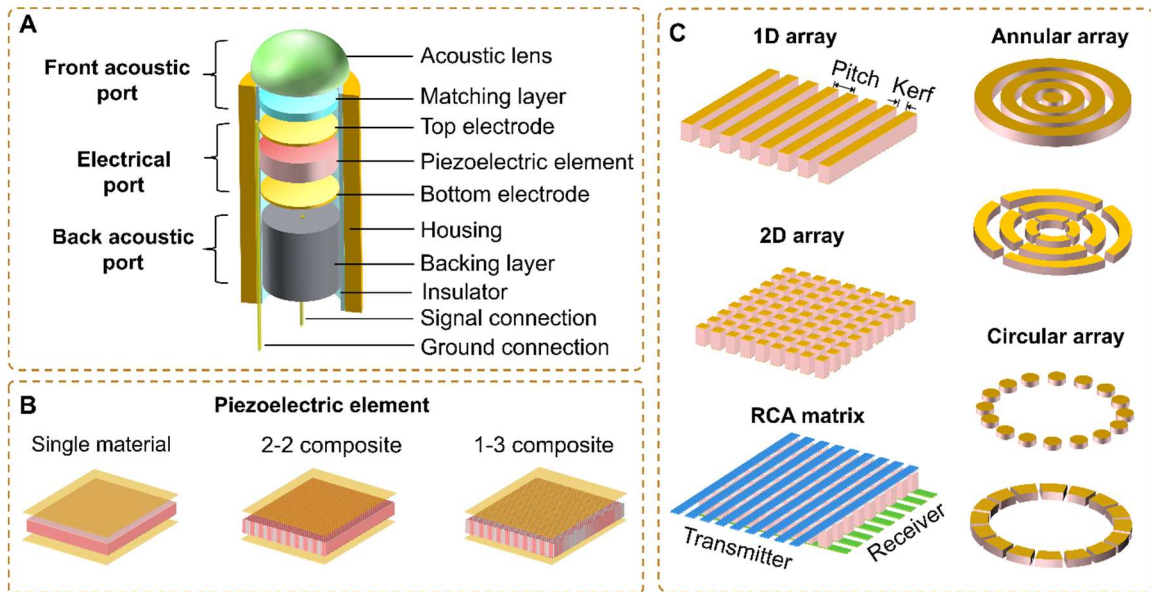
Figure 2.2 The basic information of ultrasound transducers. A) Schematic of ultrasound transducers in three port model. B) Schematic of active elements for single transducers, including single material and composites (i.e., 2-2 connection and 1-3 connection). C) Schematic of array transducers, including 1D array, 2D array, 2D array with RCA, annular array, and circular array.

Acoustic lens. Acoustic lenses have extensive applications in focused ultrasonic transducers. They serve two main purposes: i) controlling the acoustic field by focusing the ultrasound beam and generating high acoustic intensity at the focal point, and ii) safeguarding the matching layer as the lens comes into direct contact with the target in medical transducers [129]. Acoustic field regulation technology, based on piezoelectric ultrasonic transducers, can be bifurcated into active and passive control strategies. Passive control encompasses techniques such as solid curved lenses,

acoustic Fresnel lenses, acoustic projectors, liquid acoustic lenses, acoustic metasurfaces, photonic crystals, and acoustic holography [130-133]. Conversely, active control primarily involves techniques like piezoelectric arrays, piezoelectric metamaterials, and coded piezoelectric metasurfaces.[134] For example, the unique advantages of liquid acoustic lenses [133, 135], and acoustic projectors [136], are their capacity to dynamically modulate the focused acoustic field distribution by altering the volume of injected liquid and the angle of the reflective mirror. The novel acoustic hole-hologram, ensures optimal acoustic beam focusing while providing the transducer with high sensitivity [137]. Coded piezoelectric metasurfaces [138] with their dual function of sound wave generation and modulation, showcase their potential as innovative disruptors in the field of high-frequency acoustic field control.

Critical parameters. **Table 2.1** covers most of the material-related parameters because they are crucial to the transducer due to the presence of the piezoelectric element. **Table 2.2** predominantly includes data relating to transducers, such as fundamental ultrasonic concepts, transducer design, transducer evaluation, and specific resolution and Doppler parameters. The correlation between ultrasonic velocity and wavelength forms the basis of transducer design. In order to achieve a complete transmission of 100% from the transducer to the object, various equations that describe acoustic impedance and the thickness of the matching layer are commonly used for calculation purposes. The three primary criteria for assessing the acoustic performance of the transducer are the -6 dB bandwidth, insertion loss (sensitivity), and peak-to-peak voltage. The resolution of an ultrasound imaging system is heavily influenced by the design of its transducer parts, as it requires a balance between bandwidth and sensitivity. In order to produce high-quality images with detailed resolution in both the axial and lateral directions, it is necessary for the transducer elements to emit short acoustic pulses, and for the entire system to possess a high signal-

to-noise ratio and sufficient focus. Ultrasonic transducer systems have advanced to utilize linear and two-dimensional arrays, where an image is created by electronically scanning a beam. I am addressing the problem of low resolution beyond the focus plane and the limited frequency range in single-element transducer systems. Transducer performance is determined by the sound field, beam diameter, and focal zone of the single element probe. The pulse excitation and transducer parameters have an impact on the spatial resolution, temporal resolution, and contrast resolution in ultrasonic imaging.

2.2.2. Single element transducers

Single element transducers are the most common type of transducer, especially for ultrasonic imaging and diagnostic applications that require a high frequency. In the initial decades, most ultrasonic systems employed single element transducers. **Figure 2.2** B illustrate the common configuration of a single element transducer, which includes a stack comprising one piezoelectric element for converting energy, several matching layers to optimize energy transmission into the loading medium, and one backing layer to offer sturdy support for the delicate piezoelectric element and adjust the transducer's bandwidth and sensitivity. Typically, transducers that consist of only one element can be categorized as either planar or focused, depending on their specific applications [46, 47]. Focusing is utilized to enhance lateral resolution and performance in high-resolution imaging applications due to the limitations imposed by the planar construction on lateral resolution and sound intensity. A common method involves molding the piezoelectric element into a desired shape or utilizing a lens to concentrate the transducers. The primary benefit of a single-element ultrasonic transducer compared to an array ultrasound transducer is its reduced level of geometrical intricacy. Consequently, the ultrasound transducer consisting of only one element has been studied at ultrahigh frequencies (50-300 MHz).

Considering the configuration of the active layer, planar single-element transducers are commonly employed in applications requiring miniature transducers or needle transducers, such as intraoral ultrasonography [139, 140] and intravascular ultrasound (IVUS) imaging using high working frequencies (20 MHz to over 60 MHz) [141]. Intravascular ultrasound utilizes a high frequency and small aperture to accommodate the limited space surrounding the gingival area. In contrast, IVUS imaging employs side-looking single-element ultrasound transducers that are mechanically rotated by a motor within the vessel to generate a comprehensive 360-degree cross-sectional image [142]. The focused transducer configuration can improve lateral resolution and performance in high-resolution imaging applications. In some work, the focused lenses were added to achieve focused imaging without a destructive pressing effect on the piezoelectric element [143]. However, the lower sensitivity due to attenuative losses and the mechanical quality of the lens limited its practical application [144]. Recent studies have utilized innovative piezoelectric materials and composites to construct and evaluate planar single-element transducers. These transducers are commonly used to assess the performance of new materials because to their straightforward structure. It is worth noting that the reduced surface area of piezoelectric materials leads to an increased electrical resistance during the production of needle transducers [115]. Hence, the utilization of piezoelectric materials that possess significant clamped permittivity and exceptional piezoelectric characteristics is beneficial to produce needle transducers that exhibit superior performance. Extensive research has been conducted on a range of transducers consisting of elements using various piezoelectric materials, such as ceramics, single crystals, and composites.

2.2.3. Array transducers

Array transducers consist of multiple elements. These elements can have a rectangular shape and be organized in a straight line (known as a 1D linear array transducer) or have a square shape

and be organized in rows and columns (known as a 2D array transducer). They can also be arranged in a circular shape (known as a circular array), or have a ring shape and be arranged concentrically (known as an annular array) [47]. **Figure 2.2** C illustrates the schematic diagram of several array transducers. Array transducers are favored over single-element transducers in clinical applications because they offer clinical convenience, higher frame rates, and the capacity to dynamically focus the beam. An array is operated by applying repetitive voltage pulses to groups of components. A replica of the image produced by physically scanning a single transducer is generated by electronically shifting the sound beam over the front side of the transducer.

Unlike a linear array with a pitch equivalent to one wavelength, a phased array has a pitch that is less than half of that wavelength. A phased array is capable of steering beams with a reduced angular separation without generating unwanted secondary lobes known as grating lobes. Moreover, the array's comparatively smaller size is beneficial in situations where only a little contact area is permitted. A linear phased array has an element spacing of half a wavelength ($\lambda/2$) and has the ability to direct the ultrasonic beam away from the axis of the array. On the other hand, a linear array has an element separation of one wavelength in the tissue and concentrates the beam along the axis of the array. A 2D array may direct and move a beam that is focused symmetrically in order to generate a three-dimensional image across a volume. The element spacing in both dimensions is either λ or $\lambda/2$. The development of 2D matrix transducer arrays has made it possible to perform real-time volumetric imaging of entire organs on high-end ultrasound scanners, enabling therapeutic applications [145].

Table 2.2 Critical parameters and equations of ultrasound transducers [49]

Properties	Symbol	Name	Equation	Notes
Basic parameters	f	Resonance frequency of the element	$f = n\dfrac{v_p}{2t}$	v_p is the acoustic velocity of the piezoelectric element, and n is an odd integer with the lowest resonant frequency of $n = 1$
	λ	Wavelength of the transducer	$\lambda = \dfrac{v_l}{f}$	v_l is the sound velocity in the loading medium (1540 m/s for water or tissue).
	Z_m	Acoustic impedance of the matching layer (Z_p and Z_l are the acoustic impedances of piezoelectric material and the loading medium, respectively)	$Z_m = \left(Z_p Z_l\right)^{1/2}$	Single matching layer
			$Z_m = \left(Z_p Z_l^2\right)^{1/3}$	Single matching layer for wideband signal.
			$Z_{m1} = \left(Z_p^4 Z_l^3\right)^{\frac{1}{7}}$ $Z_{m2} = \left(Z_p Z_l^6\right)^{1/7}$	Two matching layers: 1st (inner) and 2nd (outer)
	t_m	The thickness of the matching layer	$t_m = \dfrac{\lambda_m}{4}$	λ_m is the wavelength in the matching layer
	f_c	Center frequency	$f_c = \dfrac{f_2 + f_1}{2}$	The center frequency of the Fast Fourier Transforms (FFT) spectrum at -6 dB
Evaluation of transducers	BW	Bandwidth	$BW = \dfrac{f_2 - f_1}{f_c}$	f_2 and f_1 is the upper and lower frequency on the magnitude of the FFT of the echo at -6 dB value, respectively.
	k_{eff}	Effective electromechanical coupling factor	$k_{eff}^2 = \dfrac{f_a^2 - f_r^2}{f_a^2}$	f_a and f_r is the anti-resonance and resonance frequency, respectively.
	IL	Insertion loss	$IL = 20\log\left(\dfrac{V_0}{V_i}\right)$	V_o and V_i are the echo voltage and excitation voltage, respectively.
	$V_{p\text{-}p}$	Peak-to-peak voltage	-	The peak-to-peak amplitude of the output voltage signal
Other performances	R_{axial}	Axial resolution (-6dB)	$R_{axial} = \dfrac{\lambda}{2BW}$ $= \dfrac{c}{2f_c \cdot BW}$	BW is the bandwidth
	$R_{lateral}$	Lateral resolution	$R_{lateral} = \lambda \cdot F_\#$ $= \dfrac{c}{f_c} \cdot F_\#$	$F_\#$ the f-number (the ratio of focal distance to aperture dimension)
	$M.I.$	Mechanical index	$M.I. = \dfrac{PNP}{\sqrt{f_c}}$	PNP is the peak negative pressure

Chapter 3   Design, Fabrication, and Characterization of the 1D Phased Array

3.1   Material selection and design of the 1D phased array

3.1.1.   Parameters of the selected piezoelectric single crystal

Piezoelectric materials play a critical role in the performance of ultrasound transducers. In previous studies, most conformable ultrasound transducers still used commercial lead zirconate titanate (PZT) ceramics [43, 44, 58, 62, 71, 146-148]. In pursuit of enhanced material properties, single crystals with morphotropic phase boundary (MPB) compositions, i.e., $Pb(Mg_{1/3}Nb_{2/3})O_3$-$PbTiO_3$ (PMN-PT), have been extensively investigated due to their high electromechanical coupling factors ($k_{33} > 85\%$) and piezoelectric coefficients (d_{33} = 1,200~2,500 pC/N) [90]. These values are far superior to those of commercial piezoelectric ceramics, such as PZT(d_{33} < 600 pC/N, k_{33} < 75%), making those materials promising candidates for ultrasonic transducers, actuators, and energy-harvesting devices [47, 93]. It has been demonstrated in bulky transducers with single elements or phased arrays, that PMN-PT single crystal based transducers exhibited enhanced acoustic performance than PZT-based transducers, including larger bandwidth, shorter pulse length, and higher axial and lateral resolution [47, 120, 121]. However, the Curie temperature T_c (~150 ºC) and rhombohedral to tetragonal phase transition temperature T_{r-t} (70-90 ºC) are quite low for PMN-PT solid solutions, which restricts their temperature usage range [90, 108]. Thus, searching for new relaxor-PT systems with i) high T_c and T_{r-t}, ii) high piezoelectric coefficients (d_{33}) are highly desired. In recent years, researchers have begun to shift their focus to crystals doped with rare-earth elements to combat this tradeoff and achieve both high T_{r-t}/T_c and d_{33} [122-124]. For example, Sm^{3+} doped PMN-PT crystals exhibited ultrahigh d_{33} (4,100 pC/N) and dielectric constant (12,000) [122], and Nd^{3+} doped PIN-PMN-PT also showed outstanding d_{33} (3,240 pC/N) and dielectric constant (9,246) [124]. However, both of them possessed lower T_{r-t} (~ 91 ºC).

Therefore, it is imperative that an investigation be performed to assess the piezoelectric properties of the new ternary system with other doping elements in order to balance both criteria.

In this work, we used a new piezoelectric single crystal, Yb/Bi co-doped $Pb(In_{1/2}Nb_{1/2})O_3$-$Pb(Mg_{1/3}Nb_{2/3})O_3$-$PbTiO_3$ (PIN-PMN-PT) system, which is provided by Prof. Dabin Lin from Xi'an Technological University. As shown in **Figure 3.1**, compared to PZT, PMN-29PT and other crystals (**Table 3.1**), the Yb/Bi-PIN-PMN-PT single crystal shows high dielectric permittivity (7500), promising piezoelectric coefficient (2800 pC/N), larger E_c (5.3 kV/cm), and higher $T_{r\text{-}t}$ (109 $^\circ$C), which make this single crystal suitable for high-voltage and high-frequency acoustic applications such as high-performance medical transducer arrays. Detailed sample preparation and characterization can be found in the article [60]. In the following work, specimens diced from the Yb/Bi-PIN-PMN-PT single crystals were used for the ultrasound transducer fabrication.
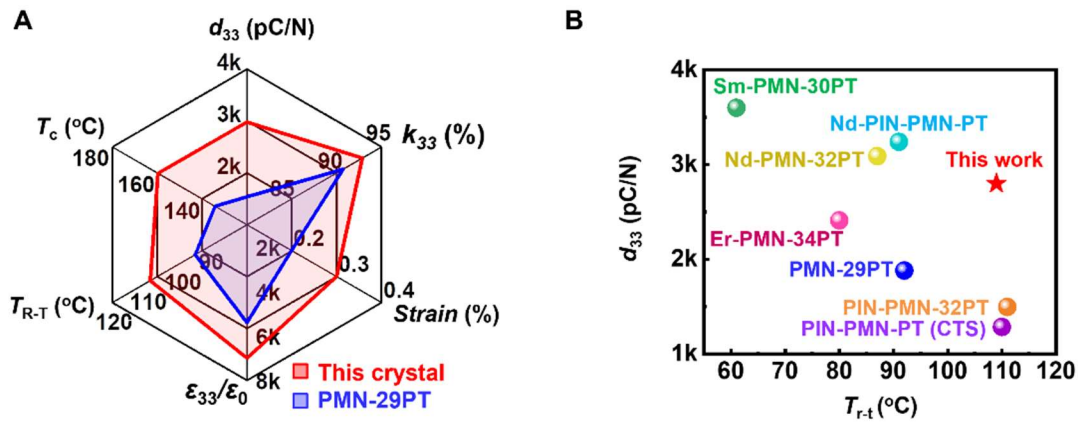
Figure 3.1 The Dielectric and piezoelectric properties of Yb/Bi-PIN-PMN-PT single crystal. A) Radar chart comparing the overall performance of Yb/Bi-PIN-PMN-PT with published results of the PMN-29PT single crystal. B) d_{33} versus $T_{r\text{-}t}$ for the Yb/Bi-PIN-PMN-PT crystals, with a comparison to other reported rare-earth–doped PMN-PT and PIN-PMN-PT crystals. The detailed comparison with reported literature and references is listed in Table 3.1.

Table 3.1 Dielectric and piezoelectric properties of Yb/Bi-PIN-PMN-PT single crystal and other published relaxor ferroelectric single crystals and PZT-5H ceramics

Single crystals	d_{33} [pC/N]	$\varepsilon_{33}/\varepsilon_0$	T_C [°C]	T_{r-t} [°C]	E_C [kV/cm]	Ref.
PMN-29PT	1881	6140	130	92	2.4	[149]
PIN-PMN-32PT	1497	4372	172	111	4.4	[150]
PIN-PMN-PT	1285	4753	155	110	4.5	[151]
Sm-PMN-30PT	3600	12300	115	61	2.6	[122]
Nd-PMN-32PT	3090	12526	138	87	2.1	[123]
Er-PMN-34PT	2410	6200	80	80	2.0	[152]
Nd-PIN-PMN-PT	3240	9246	164	91	3.3	[124]
PZT-5H ceramics	650	3800	250	-	8.0	[153]
Yb/Bi-PIN-PMN-PT	**2800**	**7000**	**160**	**109**	**5.3**	**This work**

3.1.2. Design of the 1D phased array

The 1D phased array was designed on a standard transducer three-port network [47], which includes the active piezoelectric element, backing layer, and two matching layers, depicting the geometry of the 1D phased array with its main components (Fig. 2.2A). According to the literature, the recommended transducer frequency for imaging breast tumors ranges from 5 to 12 MHz (Table 1.1). For breast scanning and imaging purposes, a 1D phased array with 64 elements a working frequency of 7.0 MHz, and the wavelength (λ) of 220 μm were chosen to strike a balance between the demands for depth and spatial resolution (Fig. 3.2). The pitch value of 125 μm (0.56λ), slightly above the phased array requirement of 0.5λ, to achieve wide-angle imaging and reduce grating lobes [154-156].
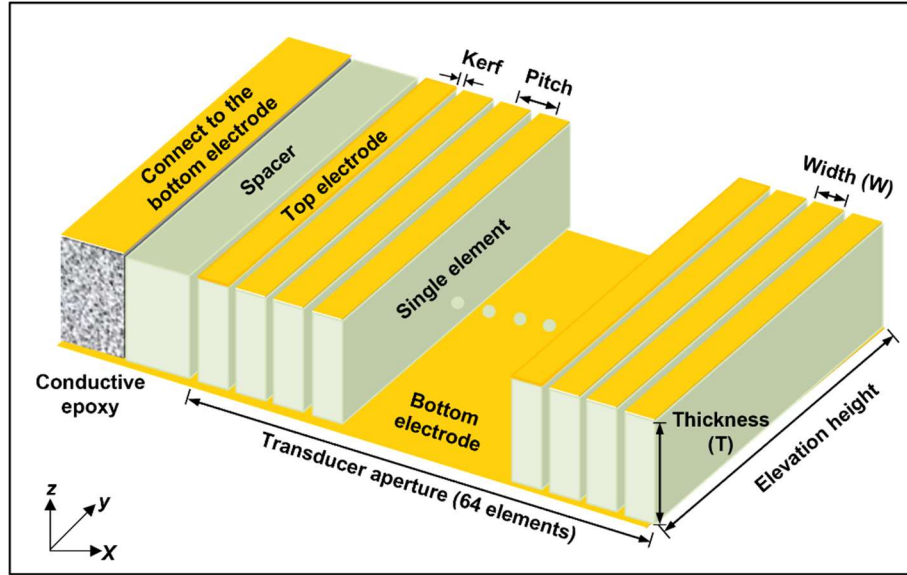
Figure 3.2 The schematic of the 1D array with key components.

According to a mode-coupling theory [157], a piezoelectric pillar's width-to-thickness aspect ratio must be lower than 0.5 to guarantee that each ceramic rod's vibration is primarily in the thickness direction and that the piezoelectric coupling factor can be used to calculate the efficiency of the device (Eq. 3-1). The longitudinal acoustic velocity and the acoustic impedance are calculated by the following equations:

$$v'_{33} = 2f_a \times t \tag{3-1}$$

$$Z'_{33} = \rho \times v'_{33} \tag{3-2}$$

where v'_{33} is the longitudinal acoustic velocity, Z'_{33} is the acoustic impedance, t is the thickness and ρ is the density of the sample. The measured dielectric, piezoelectric, and acoustic properties of the crystal are summarized in **Table 3.2**.

Table 3.2. Full matrix of material properties of the Yb/Bi-PIN-PMN-PT crystal

Elastic compliance constants s_{ij}: 10^{-12} m²/N											
Materials	s_{11}^E	s_{12}^E	s_{13}^E	s_{33}^E	s_{44}^E	s_{66}^E	s_{11}^D	s_{12}^D	s_{13}^D	s_{33}^D	s_{44}^D	s_{66}^D
Single crystal	86.1	-22.5	-61.5	130	15.8	15.3	54.1	-54.5	-8.6	19.5	14.6	15.3

Elastic stiffness constants c_{ij}: 10^{10} N/m²											
Materials	c_{11}^E	c_{12}^E	c_{13}^E	c_{33}^E	c_{44}^E	c_{66}^E	c_{11}^D	c_{12}^D	c_{13}^D	c_{33}^D	c_{44}^D	c_{66}^D
Single crystal	9.7	8.8	8.7	8.9	6.3	6.5	9.9	9.0	7.6	13.2	6.8	6.5

Piezoelectric constants: d_{ij} (pC/N), e_{ij} (C/m²), g_{ij} (10^{-3} Vm/N), h_{ij} (10^8 V/m)											
Materials	$d_{33}{}^*$	d_{31}	d_{15}	e_{33}	e_{31}	e_{15}	g_{33}	g_{31}	g_{15}	h_{33}	h_{31}	h_{15}
Single crystal	2800	-1120	240	21.8	-4.34	10.7	46.8	-23.0	6.3	19.9	-5.40	4.4

Dielectric constants: ε_{ij}, β_{ij} ($10^{-4}/\varepsilon_0$)							
Materials	ε_{11}^T	ε_{33}^T	ε_{11}^S	ε_{33}^S	β_{11}^T	β_{33}^T	β_{11}^S	β_{33}^S
Single crystal	3400	7000	2800	900	2.94	1.54	3.57	11.1

Electromechanical coupling constants: k (%)				
Materials	k_{31}	k_{33}	k_{15}	k_t	k_p
Single crystal	61	92	27	61	-

Other parameters						
	T_c (°C)	loss	ρ (g/cm³)	σ^E	g_h	Nt (Hz m)	Z (MRayls)
Single crystal	160	0.01	8.1	-	-	1800	29.2

In the transducer design for medical use, the acoustic impedance of human tissue (or water) is approximately 1.5 MRayls, which is significantly less than the acoustic impedance of the piezoelectric material [47]. Low bandwidth and sensitivity occur from a portion of the acoustic energy being lost and not being transported forward as a result. To enable the transducer's acoustic energy to travel through the body tissue smoothly and for the reflected acoustic waves (the returning echo) to return to the transducer for detection, the matching layer or layers provide the requisite acoustic impedance gradient. In this work, two matching layers were added for the array transducer. The acoustic impedance Z_{m1} (inner), Z_{m2} (outer), and thicknesses t_1, t_2 of the matching layers could be estimated using the Krimholtz–Leedom–Mattaei (KLM) model by the following equations:

$$Z_{m1} = \left(Z_p^4 Z_l^3\right)^{1/7} \tag{3-3}$$

$$Z_{m2} = \left(Z_p Z_l^6\right)^{1/7} \tag{3-4}$$

$$t_{m1} = \frac{\lambda_{m1}}{4} \tag{3-5}$$

$$t_{m2} = \frac{\lambda_{m2}}{4} \tag{3-6}$$

where Z_p and Z_l are the acoustic impedance of the piezoelectric material and load medium, respectively. λ_{m1} and λ_{m2} are the wavelengths of the acoustic wave at a center frequency in the first (inner) and second (outer) matching layers, respectively. For the Yb/Bi-PIN-PMN-PT transducer, the calculated Z_{m1} and Z_{m2} are 8.6 and 2.2 MRayls respectively according to the above formulas. The thickness of each layer is 92 μm and 98 μm, respectively. The backing layer is used to prevent the backward-emitted sound waves from echoing and ringing back into the transducer. To obtain a larger transducer's bandwidth, the acoustic impedance of the backing layer was designed to be 6.5 MRayls by comprehensively considering both bandwidth and signal amplitude. The specific design information of both array transducers was obtained by KLM simulation from PiezoCAD software (Sonicconcepts, USA).

3.2   Fabrication of the 1D phased array

The 1D phased array was fabricated and assembled at both the Center for Nanoscale Systems at Harvard University and the cleanroom facility (YellowBox) of the Media Lab at the Massachusetts Institute of Technology. Three steps were involved in the fabrication: 1) the creation of a 64-element 1D array, 2) electrode deposition and patterning followed by cable bonding, and 3) the creation of matching and backing layers.
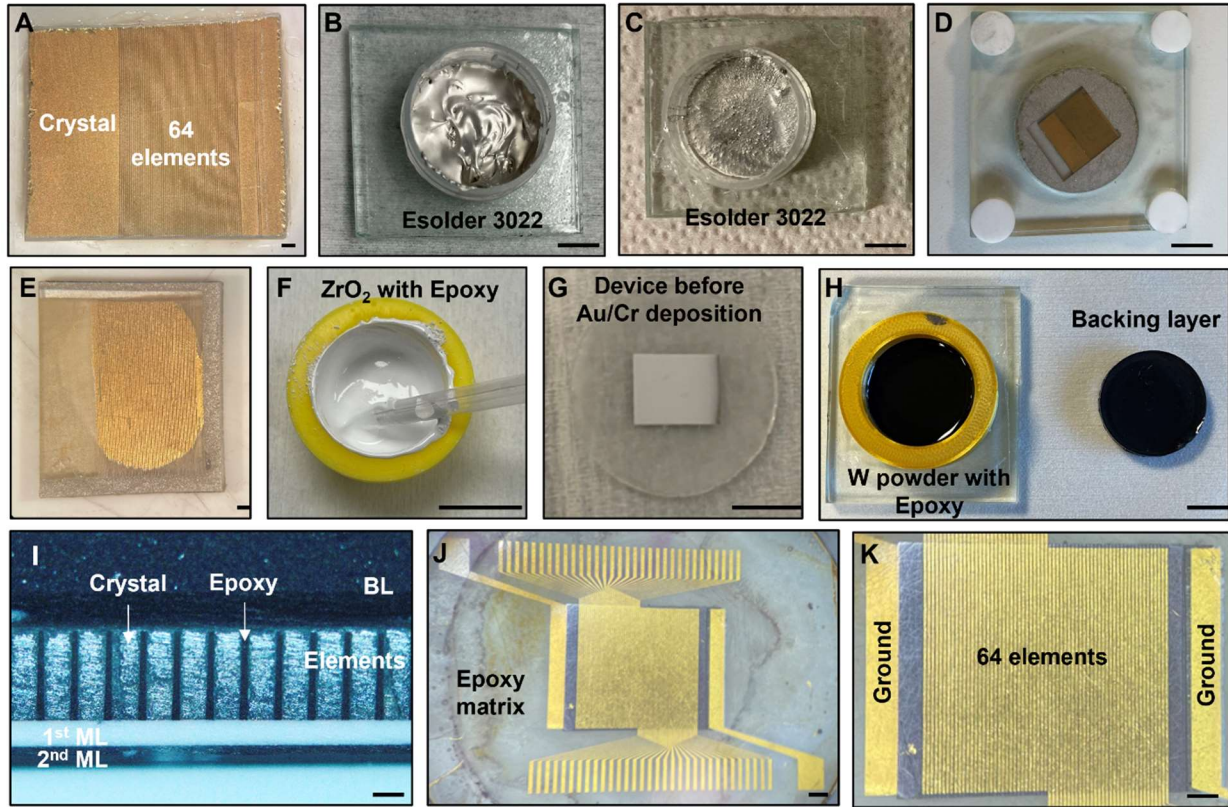
Figure 3.3 Fabrication of 1D phased array. (**A**) Single crystal piece after diced 64 elements. (**B**) Preparation of the conductive strip using Esolder 3022. (**C**) The Esolder was dried after 2 hours at 70 °C in the dam. (**D**) The polished sample exposed the diced elements. (**E**) The array with conductive strip was diced from the dam. (**F**) The preparation of the matching layer using the mixture of ZrO2 with Epoxy. (**I**) The optical microscopy image of the array's cross-section, including 1st and 2nd matching layer (ML), piezoelectric elements, and backing layer (BL). (**J**) The photo of the top electrodes on the array. (**K**) The zoom-in view of electrode traces on the array elements. 1 mm (A, E, J, K), 1 cm (B, C, D, F, G, H), 0.1 mm (I).

3.2.1. Fabrication of 64-element array

The traditional dice-and-fill method was used to fabricate the 1D phased array. To achieve 65 dicing lines on the sample (**Fig. 3.3A**), a dicing machine (DISCO, Tokyo, Japan, Model DAD 321) with a 15 μm-thick synthetic diamond blade (DISCO, Tokyo, Japan, Z09-SD3000-Y1-60) was utilized. To increase the crystal footprint and minimize damage from blade vibration, our research lab generated the appropriate specifications for DISCO to custom manufacture the ultra-thin dicing

blade. The dicing pitch, kerf, and actual width of each element were 125 μm, 30 μm, and 95 μm, respectively. To avoid any mechanical harm to the elements, the dicing speed was fixed at 0.25 mm/s. The dicing depth was roughly 350 μm, which was greater than the final desired thickness to allow for further polishing. The epoxy (EPO-TEK 301, Epoxy Technology Inc. USA) was used to fill the kerf and eliminate the transverse vibration in the ceramic by vacuum degassing and was cured at 65 °C for 2 hours. After lapping the top surface to expose ceramic elements, the conductive epoxy strip (E-SOLDER 3022, Von Roll USA, Inc.) was added on both sides to connect the bottom electrode to the top surface (**Fig. 3.3B-C**). Finally, the entire array was polished to the designed thickness and encapsulated by epoxy again in a round mold (**Fig. 3.3D-E**).

3.2.2. Preparation of matching layers and backing layer

The final array was obtained by adding the matching layer and the backing layer. For the matching layer preparation, the Zirconia oxide powder (5 μm, 99%, CAS-No.: 1314-23-4, Sigma-Aldrich Inc.) was selected as the filler and the Epoxy (EPO-TEK 301, Epoxy Technology Inc. USA) was used as the matrix. The ZrO_2 powder and epoxy solution were first mixed with a ratio of 3:1 to obtain a homogenous mixture, poured into the mold, centrifuged at 2000 rpm for 10 minutes, and then cured at 65 °C for 2 hours in the oven (**Fig. 3.3F**). After polishing the 1st matching layer to the designed thickness, the epoxy solution was cast on the surface of the 1st matching layer and polished to achieve the 2nd matching layer (**Fig. 3.3G**). For backing layer preparation, the Tungsten (W) powder (APS 1-5 micron, 99.9%, CAS No.: 7440-33-7, Alfa Aesar) was selected as the filler, and the Epoxy (EPO-TEK 301, Epoxy Technology Inc. USA) was used as the matrix. The W powder and epoxy solution were first mixed with a ratio of 4:1 to obtain a homogenous mixture, which was poured into the mold, centrifuged at 2500 rpm for 10 minutes, and then cured at 65 °C for 2 hours in the oven. The final backing layer was obtained by polishing

the surface to the designed thickness (**Fig. 3.3H**). Finally, the matching and backing layers were bonded onto the array by the epoxy solution. Firm pressure was applied to the bonding area, which was then cured in the oven at 65 °C for 1 hour.

3.2.3. Electrode patterning

The chromium (Cr, 10 nm) and gold (Au, 300 nm) were deposited on the upper surface of the array by e-beam evaporation (Denton electron beam deposition). A layer of photoresist (AZ 5214-E IR, MicroChem Corp.) was spin-coated onto the electrode at a speed of 3,000 rpm for 60 seconds and then baked at 65 °C for 10 minutes. Then the array was UV exposed for 10 seconds under a Mask Aligner (MJB4, SÜSS MICROTEC SE, Germany), developed for 60 seconds in a developer (MIF AZ 726, MicroChem Corp.), and then wet etched by Au and Cr etchant solution for 120 seconds and 20 seconds, respectively. After stripping with acetone, IPA, and deionized (DI) water, the final electrode pattern on the top surface is completed, including 64 traces of electrodes and two wide traces on strips of E-Solder 3022 (**Fig. 3.3J-K**). Finally, the chromium (Cr, 10 nm) and gold (Au, 300 nm) layers were deposited on the bottom surface of the array by e-beam evaporation again. The bottom electrode fully covered all elements and strips of E-solder 3022.

3.2.4. Electrode bonding and device packaging

The cross-sectional view reveals of the device that the epoxy solution under high-temperature pressure has firmly bonded all of the components, giving them a consistent thickness (**Fig. 3.3I**). The ACF cable was bonded to the array and the printed circuit board (PCB) interface under a microscope. To avid the electric short circuit, the exposed areas were fully covered by the Kapton tape. The bonding area was applied with strong pressure and cured in the oven at 65 °C for 1 hour. After bonding with matching layers, the backing layer, and the anisotropic conductive film

(ACF) cable (**Fig. 3.4**), the thickness of the entire device is still less than 3 mm. The tracker was bonded on the backing layer to hold the device.
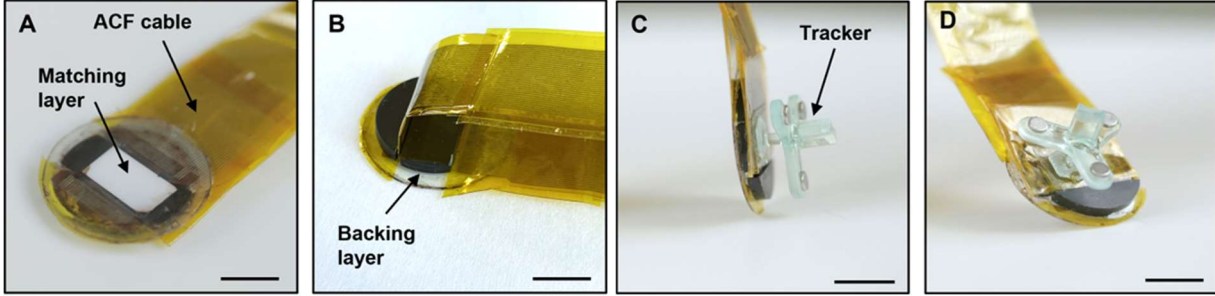
Figure 3.4. Different views of the 1D phased array with the tracker and ACF cable. (**A**) The view from the top side. The white area is the 1st matching layer, which is covered by the 2nd transparent matching layer. (**B**) The view from the backside. The thick black piece is the backing layer. (**C**) Side view of the device. The backing layer is under the top ACF cable. (**D**) The view of the backside with the tracker. Scale bar, 1 cm (A-D).

3.3   Characterization and performance of the 1D phased array

3.3.1. Electrical performance of the elements

The electrical impedance of the diced elements and the fabricated array were measured in the air at room temperature using an impedance analyzer (Agilent E4991A, Agilent Technologies, Santa Clara, CA, USA). Two key parameters, resonance frequency (f_r) and anti-resonance frequency (f_a), can be obtained from the impedance spectrum. The thickness electromechanical coupling coefficient (k_t) and effective electromechanical coupling coefficient (k_{eff}) are calculated with the following formula:

$$k_{eff} = \sqrt{\frac{f_a^2 - f_r^2}{f_a^2}} \qquad\qquad (3\text{-}7)$$
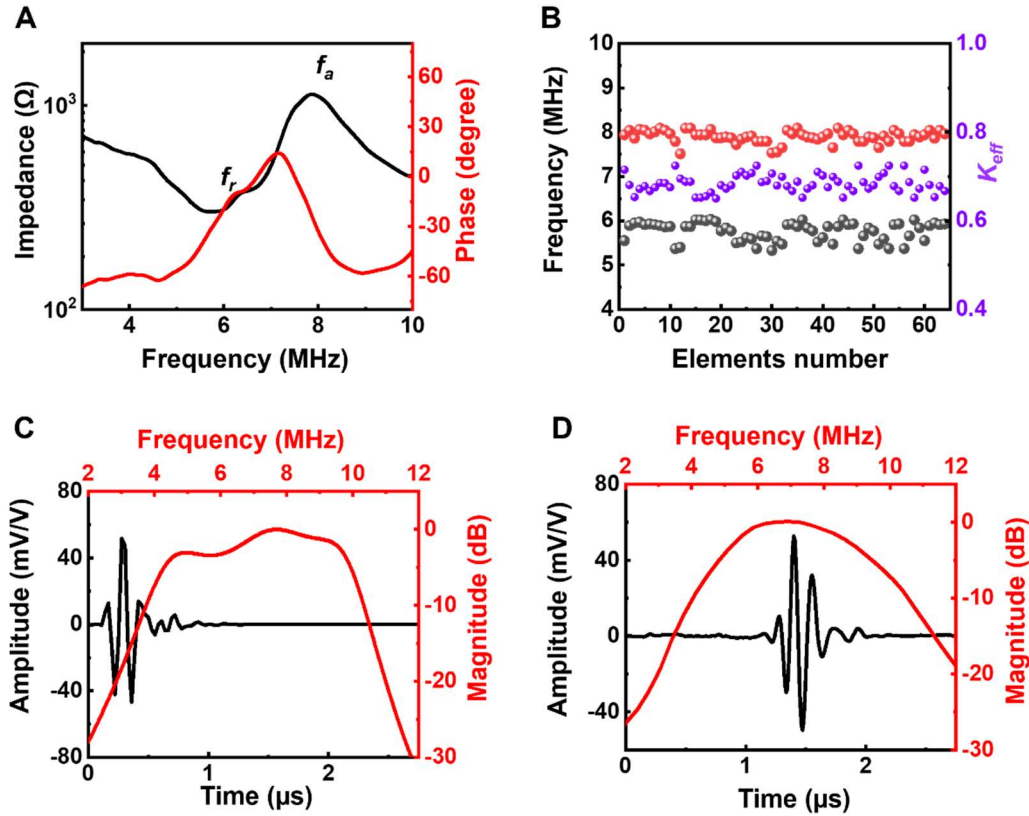
Figure 3.5. The piezoelectric and acoustic performance of 1D phased array. (A) Electrical impedance spectrum of a single element of the phased array. **(B)** The resonance frequency, antiresonance frequency, and electromechanical coupling coefficient of 64 elements of the phased array. **(C)** The two-way pulse-echo impulse response simulated the results of one element by the KLM model **(D)** The measured waveform and frequency spectrum of the single element of the phased array.

For acoustic testing to obtain the bandwidth, a pulser/receiver (JSR Ultrasonics DPR 300) was used to individually excite single elements from the transducer with a voltage of 100 V, then received by the element itself. A large disk of quartz was located in the water tank for reflection. The relative position between the array and the quartz was adjusted to achieve the strongest signal. The two-way echo response was captured by the element itself and displayed on an oscilloscope (PicoScope 5444B), while the frequency domain was calculated by fast Fourier transform (FFT). The center frequency f_c and -6 dB bandwidth (BW%) were calculated by:

$$f_c = \frac{f_1+f_2}{2} \tag{3-8}$$

$$BW\% = \frac{f_2-f_1}{f_c} \times 100\% \tag{3-9}$$

where the f_1 and f_2 are the frequency when the magnitude of the FFT of the echo at -6 dB value, and f_1 is smaller than f_2.

The frequency dependence of electric impedance and phase of a single element is shown in **Fig. 3.5A.** The resonance and anti-resonance frequencies are 5.9 MHz and 8.1 MHz, respectively, resulting in a large effective electromechanical coupling coefficient (k_{eff} = 0.68). The array also showed a -6 dB bandwidth of 70% with the center frequency around 7.1 MHz (**Fig 3.5C**), which is slightly smaller than the simulation results (79% in **Fig 3.5D**) by the Krimholtz–Leedom–Mattaei (KLM) model due to the fabrication processing, flexible cable, or unmatched electric circuit. In addition, the array's electrical impedance and acoustic performances were measured to investigate the uniformity of array elements. The performance of all elements of the array is shown in **Fig. 3.5B**.

3.3.2 Connections and beamforming information

To enable real-time imaging, a data acquisition interface connected the array to a Vantage 256 system (Verasonics, Inc.). The array was tested on two different phantoms to quantify their acoustic performance and imaging capacity prior to conducting human clinical trials.

The data acquisition process was conducted utilizing the Vantage 256 ultrasound system, which is equipped with a sufficient analog front-end for transmitting and receiving on a maximum of 256 channels simultaneously. To establish a connection between the manufactured transducers and the Vantage 256 system, a universal transducer adapter (UTA)-compatible adaptable connector

was conceptualized and constructed. **Fig 3.6** delineates the signal path and overall configuration from the transducer to the system. To begin, a Philips ATL C5-2v ultrasound transducer probe, which has the capacity to support a maximum of 128 individual elements, was dissected. Following the process of detaching from the initial printed circuit board (PCB), a multimeter was employed to verify the connection of each signal line to its corresponding port in the UTA. It is noteworthy to mention that the arrangement of the UTA connector does not adhere to the physical structure of a transducer in a sequential fashion. In accordance with the arrangement of the components in the UTA connector, individual cables were soldered onto PCB II. The final design for PCB II organized these cables into eight groups of sixteen lines, rerouted the signals to match the UTA connector's expectations, and utilized sequential ordering at its inputs. To facilitate the interchangeability of the transducer, ribbon cables connected PCB II to PCB I, which was complementary to the transducer. Given that each transducer is composed of 64 elements, this interface permits the parallel connection of two transducers.

A conventional focused beamforming method was utilized to perform real-time imaging. The transmission delays were configured to sweep across a range of ±45 degrees using 128 lines. The imaging depth was configured to 60 mm, while the transmit focus was set at 50 mm. The transmitted excitation consisted of a single-cycle sine wave with an amplitude of 50 volts and a central frequency of 7.0 MHz. The image dynamic range was adjusted to 60 dB. The technique employed was triangular apodization, which enhances spatial resolution significantly while also minimizing sidelobes to a level of -27 dB. The time-gain control (TGC) was manually modified to rise as the depth increased. This adjustment reduced the strength of signals near the array while enhancing signals further away from the array, resulting in a more consistent level of brightness in the image. In post-processing, a Python script was used to crop the video to show just the

ultrasound image, then the image dynamic range was rescaled as desired. Generally, the dynamic range was rescaled to 55 dB, since higher dynamic ranges begin to show the noise floor.
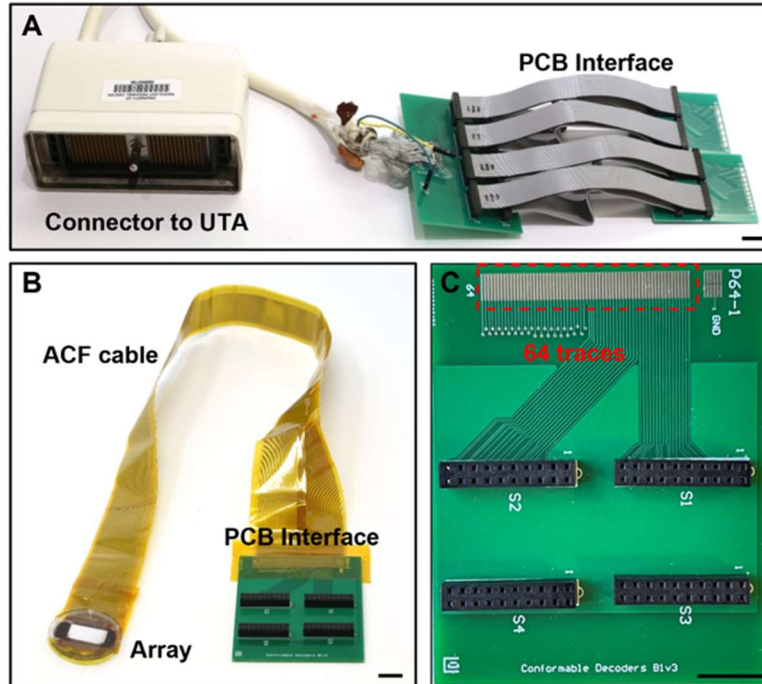
Figure 3.6. The 1D array and electrical connection for imaging. (**A**) Modified array-to-system connection. (**B**) The array with cable and PCB interface. (**C**) The PCB interface with 64 traces and ground electrode connections. Scale bar, 1 cm.

3.3.3. Imaging performance of 1D ultrasound arrays on phantoms

First, a planar ultrasound phantom with wire and cylinder targets (model 040GSE, Computerized Imaging Reference Systems, Inc.) was utilized to demonstrate the field of view and resolution (**Fig. 3.7A-B**). The 2D images on vertical and horizontal distance targets, axial and lateral resolution targets, and hyperechoic/hypoechoic targets were obtained. The results demonstrate that the phased array has a maximum field of view of up to 100 mm width and an imaging depth of approximately 80 mm (**Fig. 3.7C**). For the resolution targets at 30 mm depth, the array separated targets with gaps as small as 0.25 mm in the axial direction and 1.0 mm in the

lateral direction, indicating a promising resolution for soft tissue imaging under skin around 30 mm (**Fig. 3.9A-D**). In addition, hyperechoic/hypoechoic targets can be used to determine the minimum contrast sensitivity of the array. The images on different grayscale targets from +15 dB to -9 dB are at the depth of 30 mm as shown in **Fig. 3.8E**. The results indicate that the 1D array can clearly identify the lowest contrast targets with -3 dB and +3 dB in this phantom, which demonstrates the sufficient contrast sensitivity (~ 3 dB) of this 1D array [146, 154].
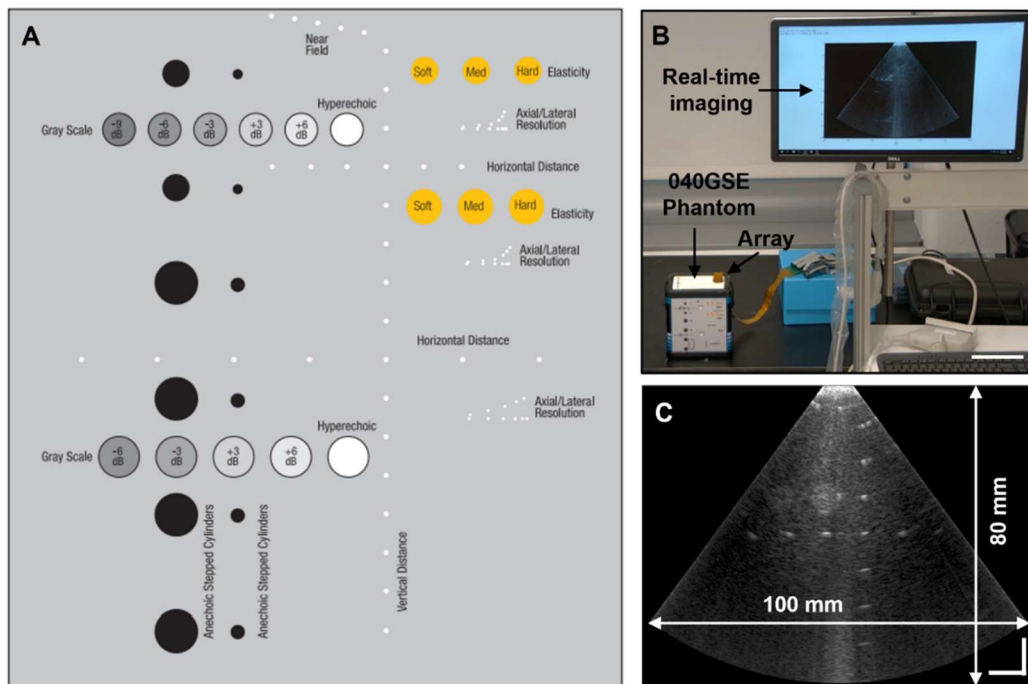
Figure 3.7. Real-time imaging on the ultrasound phantom (model 040GSE). (**A**) The schematic of various targets in the phantom (from the website of the product). (**B**) The real-time imaging on the 040GSE phantom. (**C**) The 2D image on vertical and horizontal distance targets to show the field of view and maximum depth. Scale bar, 10 cm (**B**) and 1 cm (**C**).
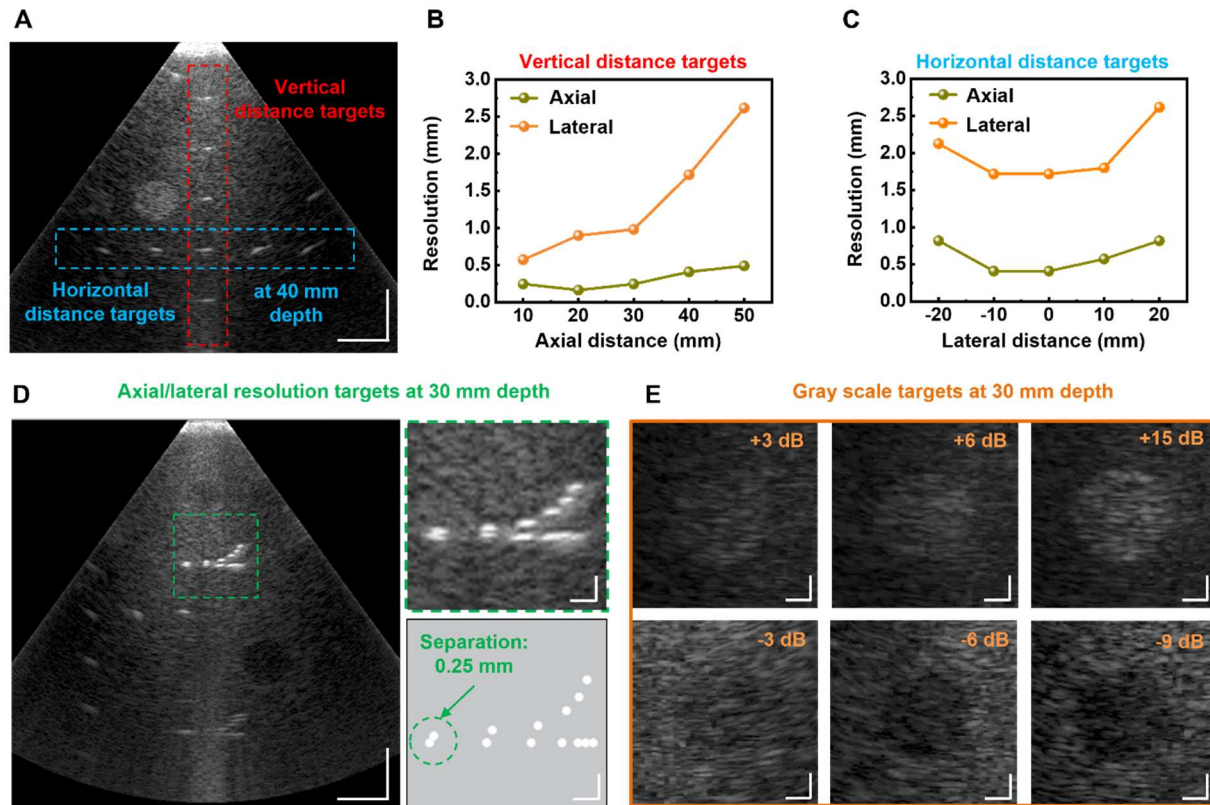
Figure 3.8. Imaging resolution analysis. (**A**) The ultrasound image of vertical distance targets (red dashed area) and horizontal distance targets (blue dashed area). (**B**) Lateral and axial resolutions of the 1D array at different depths. (**C**) Lateral and axial resolutions of the 1D array with different lateral distances from the central axis. (**D**) The ultrasound image of axial/lateral resolution targets at 30 mm. The zoom-in view green dashed area in (**D**) and the schematic of the axial/lateral resolution targets indicate the separations between targets. (**E**) The ultrasound images of the grayscale group at 3 cm depth with hyperechoic targets (+3 dB, +6 dB, and +15 dB) and hypoechoic targets (-3 dB, -6 dB, and -9 dB). Scale bar, 1 cm (A, D) and 2 mm (E).

To further evaluate the imaging quality of the cUSBr-Patch on a curved surface, the oval phantom (Model US-18, Kyoto Kagaku CO.LTD) was used (**Fig. 3.9**). Six individual images were taken that depict a large sphere object, a tube object, a bean-shaped object, and a square pyramid object, a cylinder object, and a cubic object in different depths and locations both clearly and distinctly.
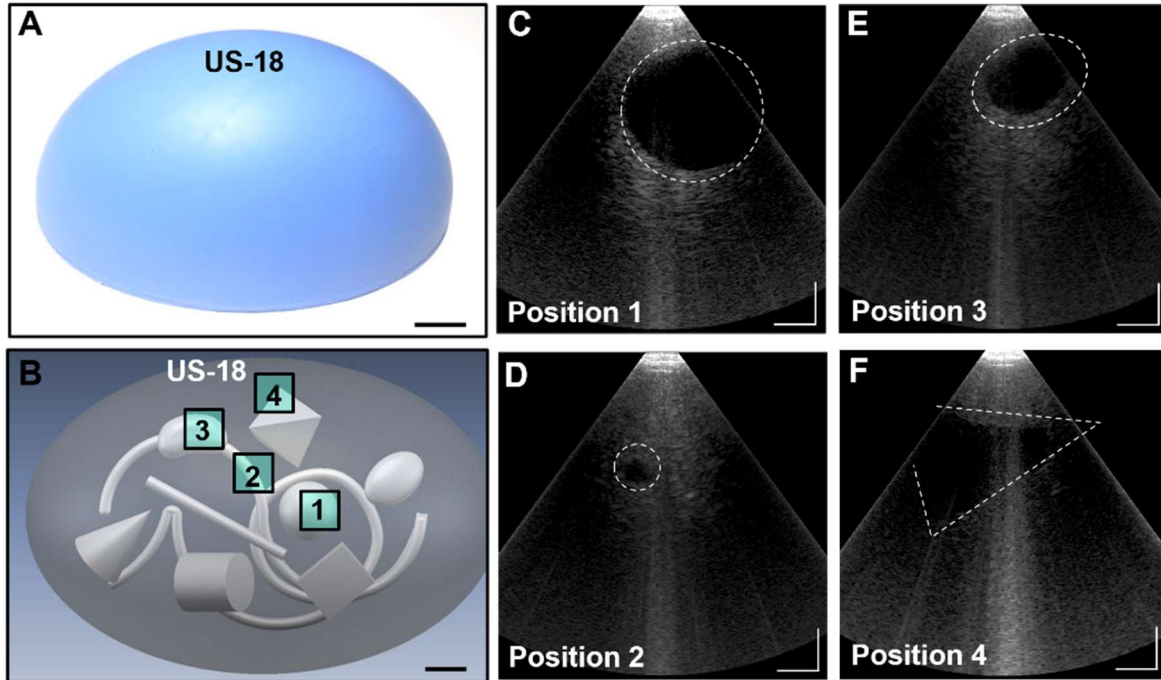
Figure 3.9. Imaging on the oval phantom (Model US-18, Kyoto Kagaku CO.LTD). (**A**) The photo of the oval phantom. (**B**) The schematic of the top view of the oval phantom and embedded 3D objects. Four squares indicate the location of the array. (**C-F**) 2D images on a large sphere object, a tube object, a bean-shaped object, and a square pyramid, respectively. The white dashed lines indicate the shape and location of each object. Scale bar, 1 cm.

Chapter 4   Clinical Study on Breast Tissue Imaging

4.1   The clinical study on the subject

4.1.1. The nature-inspired patch for clinical study

The design and fabrication of the cUSBr-Patch were led by the team member Emma Suh. Avani Ahuja, Lin Zhang, and I participated in the whole process from the idea proposal to the fabrication of the final version. The aim of the design was to create a wearable interface that connects a 1D array to breast tissue, ensuring the array is consistently positioned and oriented in different areas of the breast (**Fig. 4. 1A**). The honeycomb patch design, which takes inspiration from nature, consists mostly of three components (**Fig. 4.1B**): i) A soft textile bra to act as a familiar intermediate layer, ii) a honeycomb patch as the outer layer to offer support and direction for the 1D array, and iii) the tracker connected to the ultrasound array for managing and rotating the array at a certain position. The rectangular magnets from LOVIMAG and the circular magnets from Linlinzz are utilized to affix the patch onto the bra and secure the tracker onto the patch apertures, respectively.

The Barely Zero fabric bra from NEIWAI is designed without any seams, providing comprehensive coverage for a diverse range of breast sizes, from A to DD. The rectangular magnets (**Fig. 4.1B**) were strategically positioned and fastened in the most advantageous locations to ensure that the outer patch could securely adhere to the bra in the proper alignment. This feature enabled the cable of the 1D array to have unrestricted movement while smoothly sliding between the magnets. We created circular apertures in the bra that corresponded with the patch's openings, allowing the array to make direct contact with the skin (**Fig.4.1J**). The patch's symmetrical construction allows for the bra to be inverted, enabling the application of the ultrasound technique

to the other breast. The patch, designed with a honeycomb pattern, includes open sections that enable the tracker to move freely along a predetermined path (**Fig. 4.1D**), thereby maximizing its field of vision. The patch was developed taking into account four primary factors: i) user-friendliness, ii) full range of motion (360° rotation at a specific place with consistent array localization), iii) environmentally-friendly production, and iv) user comfort. Existing ultrasound devices do not have the necessary accessibility and operational ease for all users. However, the honeycomb patch offers a close and user-friendly interface that enhances the reliable functioning of the ultrasound array. The honeycomb design, which takes inspiration from nature, was generated using Autodesk Fusion 360.

Honeycomb structures are favored in medical devices due to their ability to reduce material usage during manufacturing, enhance flexibility, effectively cover extensive skin areas, and provide structural stability. These properties enable the patch to conform to the body and allow for customized array scanning [158, 159]. The patch, which is 2 millimeters thick, consists of a white thermoplastic polyurethane (TPU) layer and a gray polylactic acid (PLA) layer. This combination allows the patch to contour to the body while maintaining a strong and solid structure (**Fig. 4.1E**). There are six apertures in the patch that allow the tracker to rotate a full 360 degrees (**Fig. 4.1G-I**). In addition, the tracker has the capability to move along a path consisting of a maximum of 15 hexagonal sections (**Fig. 4.1D**). This allows for a basic scanning process to accurately locate the lesion, going beyond the usual four-quadrant identification (**Fig. 4.1C-E**). The collective range of perspectives provided by each aperture adequately encompasses the pertinent regions of the breast, facilitating a thorough collection of superimposed ultrasound images.
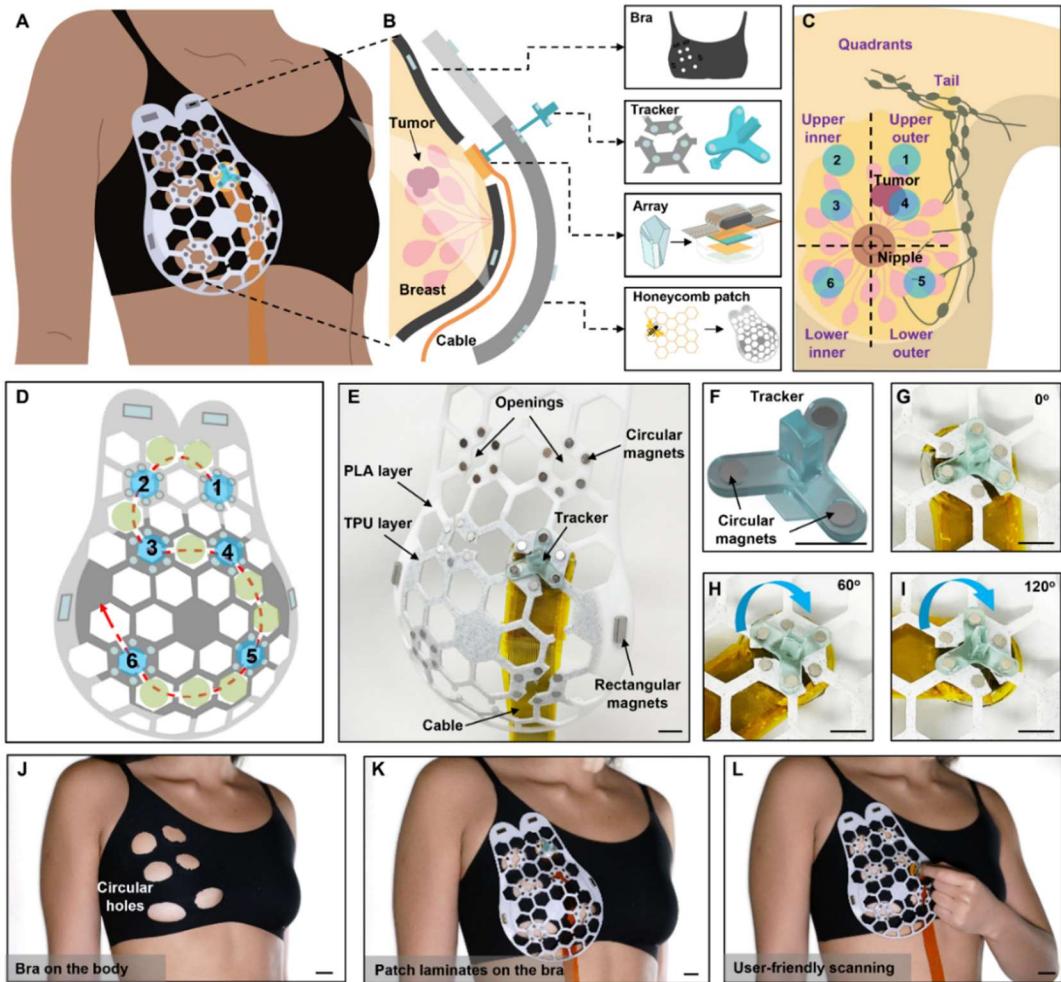
Figure 4.1. The overview of the design of the cUSBr-Patch. (**A**) Schematic of a cUSBr-Patch on the body. (**B**) Exploded view of the cUSBr-Patch to illustrate its four main components: a soft fabric bra to serve as a familiar intermediary layer, a honeycomb patch as the outside layer to provide structure and guidance of the 1D array, the tracker to hold and rotate the 1D array, and the single crystal–based 1D phased array. (**C**) Schematic of breast quadrants and the positions of circular regions that align with the patch openings and circular holes in the bra. (**D**) Schematic of the honeycomb patch with six main openings (blue areas). The red dashed line indicates the specific trace for the 1D array scanning. The light green areas indicate an additional nine hexagonal sections for imaging. (**E**) Photo of the honeycomb patch with the array and tracker. (**F**) Photo of the tracker. (**G** and **I**) Photos of the tracker rotating clockwise from 0° to 120°, demonstrating its capability for a 360° rotation. (**J**) Photo of the fabric bra with circular holes on a healthy human subject. Circular holes are designed to specifically serve as openings for the array to have intimate integration with skin and align with patch openings. (**K**) Photo of the patch attaching to the bra without mechanical delamination. (**L**) Photo of an easy-to-operate scanning. Scale bars, 1 cm (E) to (I) and 2 cm (J) to (L).

The tracker is affixed to the 1D array to facilitate insertion into specified imaging spots and has the ability to move unrestrictedly within the patch (**Fig. 4.1D and F**). The circular magnets were affixed to their respective locations within the patch by inserting them into the circular press-fit notches (**Fig. 4.1E**). The circular magnets contained in the patch determine six primary positions for the tracker, each spaced 60 degrees apart (**Fig. 4.1G-I**). The openings in the patch are strategically positioned to align with the round holes in the bra, allowing for the precise insertion of the round magnets. The tracker has three prongs that are evenly spaced from each other. Each prong has a circular pocket where a round magnet can be inserted. The integration of the array with the tracker enables the tracker to remain consistently positioned between the skin and the patch (**Fig. 4.1K**). The tracker is equipped with a handle on its top, which enables the user to firmly hold and manipulate it (**Fig. 4.1L**). The detailed fabrication steps can be found in the Science Advances article [60].

4.1.2. The preparation of IRB documentation

The operations performed on individuals having a history of breast anomalies were carried out in compliance with the authorized experimental protocol by the Committee on the Use of Humans as Experimental Subjects of the Massachusetts Institute of Technology (COUHES, No. 2011000271).

To be eligible for Group I (<u>subject with the health condition of the breast</u>), the subject must:

1) Be between 18-85 years old.
2) Not be pregnant.

3) Not having significant health problems (such as chronic or acute cardiovascular diseases, skin diseases) physical and/or behavioral health disabilities limiting your ability to follow directions and complete research-related activities.

4) Be healthy (self-report), BMI between 17 and 40.

5) Be able to walk briskly at least one block without difficulty and not experience shortness of breath at a normal walking pace rate (> 2 mph).

6) Be able to understand, communicate, give valid consent to the study, and be understood by researchers.

 To be eligible for Group II (<u>subject with breast anomaly history</u>), the subject must:

1) Be between 18-85 years old.

2) Has the following unhealthy breast or related problems (such as breast pain, breast tenderness, gynecomastia, tumors, cysts, fibroadenomas, fat necrosis, sclerosing adenosis, generalized breast lumpiness, etc.)

3) Not be pregnant.

4) Not have other significant health problems (such as chronic or acute cardiovascular diseases, skin diseases) physical and/or behavioral health disabilities limiting your ability to follow directions and complete research-related activities.

5) Be healthy (self-report), BMI between 17 and 40.

6) Be able to walk briskly at least one block without difficulty and not experience shortness of breath at a normal walking pace rate (> 2 mph).

7) Be able to understand, communicate, give valid consent to the study, and be understood by researchers.

The participants duly filled out the informed consent forms. The inclusion criteria encompassed individuals who identified as female, aged between 18 and 85 years, and had a body mass index ranging from 17 to 40 kg/m^2. Participants were disqualified if they had notable health conditions (such as chronic or acute cardiovascular diseases, or skin disorders) or physical and/or behavioral limitations that hindered their ability to comply with instructions and carry out research-related tasks. Subjects may have several breast-related ailments, including breast pain, breast tenderness, tumors, cysts, fibroadenomas, fat necrosis, sclerosing adenosis, and widespread breast lumpiness.

4.1.3. The procedure of clinical study

The clinical investigation took place at the MIT Center for Clinical and Translational Research (CCTR) (**Fig. 4.2A**). The imaging procedure was conducted using the Vantage 256 system, initially with the cUSBr-Patch. Subsequently, it was validated using a clinical GE Logiq E10 (GE Healthcare, Waukesha, WI) equipped with a linear probe (GE ML6-15). The acoustic coupling was achieved using Scan 11-08 Ultrasound Gel from Parker Laboratories, Inc. This investigation was supported by two clinical research nurse coordinators from the MIT CCTR and one clinical applications specialist from GE Healthcare.

A participant, aged 71, with a BMI of 37 and a history of abnormal breast conditions, was enrolled. The participant was instructed to lie flat on an examination table and arrange her garments to allow ultrasonic scanning of her breasts. Initially, we employed a phased array to perform a clockwise scan of the subject's breast, starting from the outer edge and moving toward the nipple. Subsequently, we identified the lesion and conducted scans in three distinct orientations. Second, the subject was asked to wear the designed bra and patch. Subsequently, we conducted a second scan of the breast at six distinct sites in accordance with the patch design (**Fig. 4-2B**). In order to

validate the imaging, the specialist employed the GE ML6-15 probe to scan the subject's breast in a clockwise direction from the outside border to the nipple, after removing the bra and patch. This scan successfully identified and determined the sites of the lesions. Ultimately, the ultrasonic gel was removed from the subject's skin using a clean wiper.
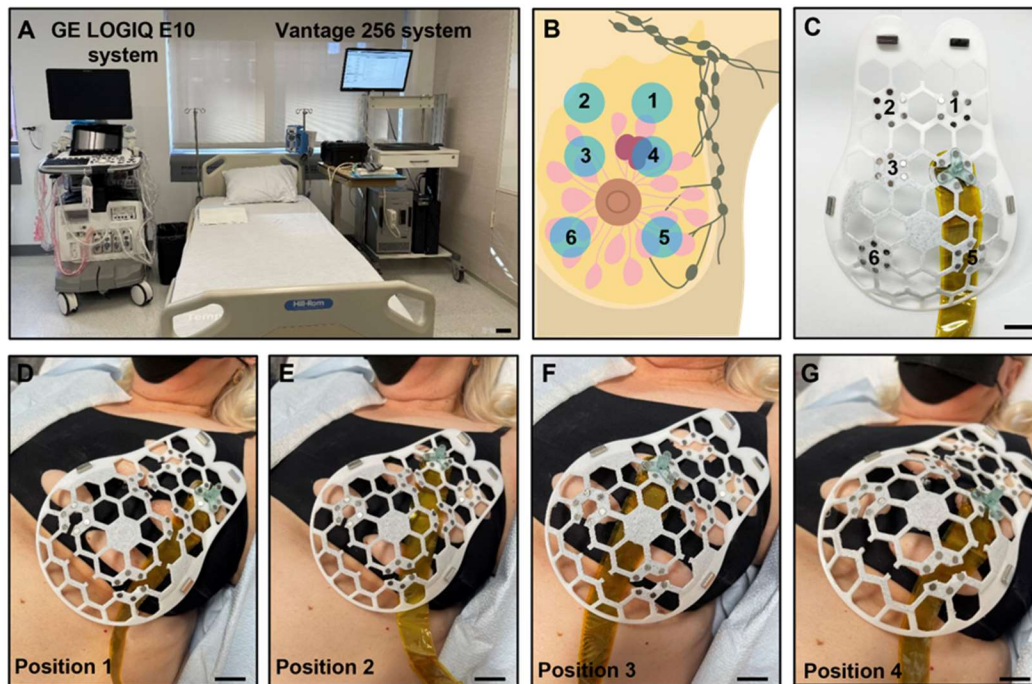
Figure 4.2. The *in vivo* study on breast tissue. (**A**) The study room for the clinical trial at the MIT CCTR, including the GE Logiq E10 system, the Vantage 256 system, and an examination table. (**B**) The schematic of the breast with a cyst and the cUSBr-Patch with six openings for imaging. (**C**) The photo of the cUSBr-Patch before the clinical study. (**D-F**) The photos of the cUSBr-Patch on the left breast of the subject and the array at different positions. Scale bar, 10 cm (A) and 2 cm (C-G).

4.2   Results and Discussion

4.2.1. The breast tissue imaging

The ultrasound images at different positions with initial 0° orientation to 60° and 120° were collected via the Vantage 256 system. All B mode images are directly cropped from the video, without any post-processing.
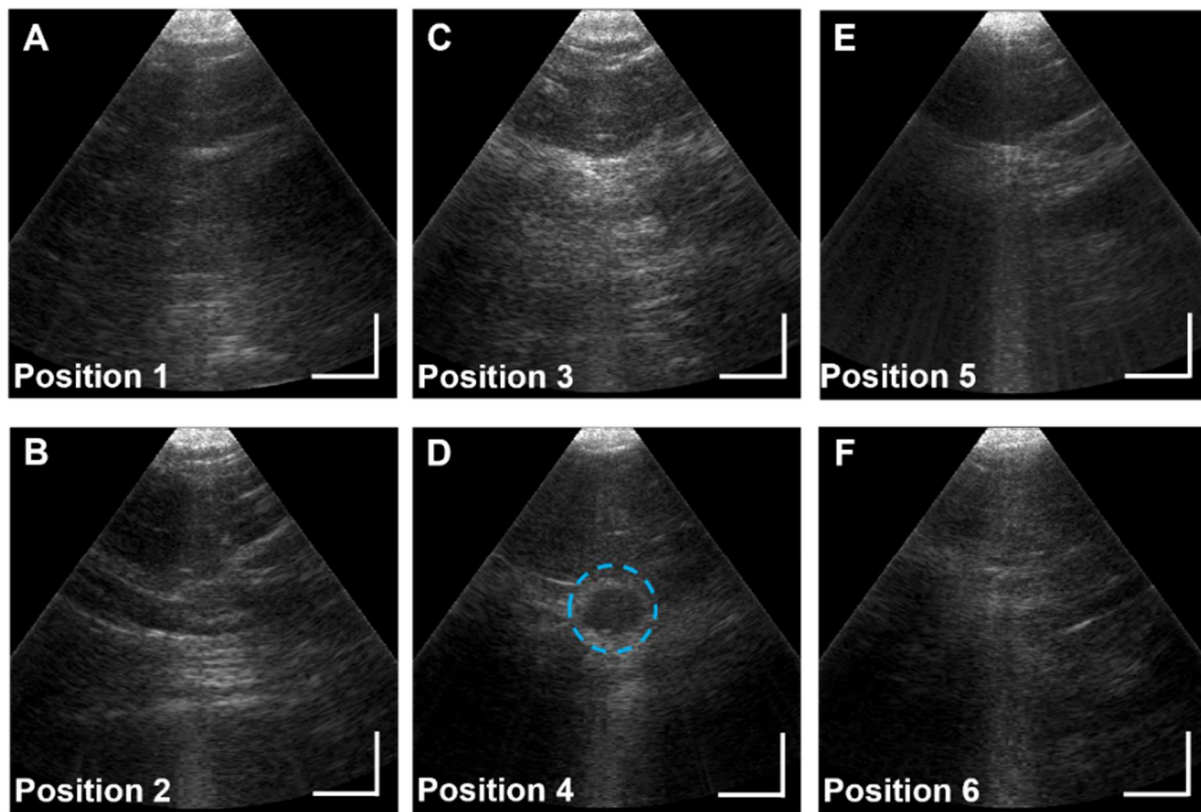
Figure 4.3. The ultrasound breast images at Position 1 to 6 (A-F). Scale bar, 1 cm.

Fig. 4.3 B shows the patch on the left breast and the scan sequence from Position 1 to 6 along the designed trace in the patch (**Fig. 4.1D**). Thanks to the reasonable maximum image depth and axial/lateral resolution, we can clearly observe various breast tissue from different positions (**Fig. 4.3**). At Position 4, a cyst with a diameter of 1 cm can be detected, which appears as well

circumscribed and hypoechoic due to the lower acoustic impedance than the surrounding tissues. To better define the lesion shape, the array at Position 1-4 was rotated by manipulation of the tracker from its initial 0° orientation to 60° and 120°, respectively (**Fig. 4.4**).
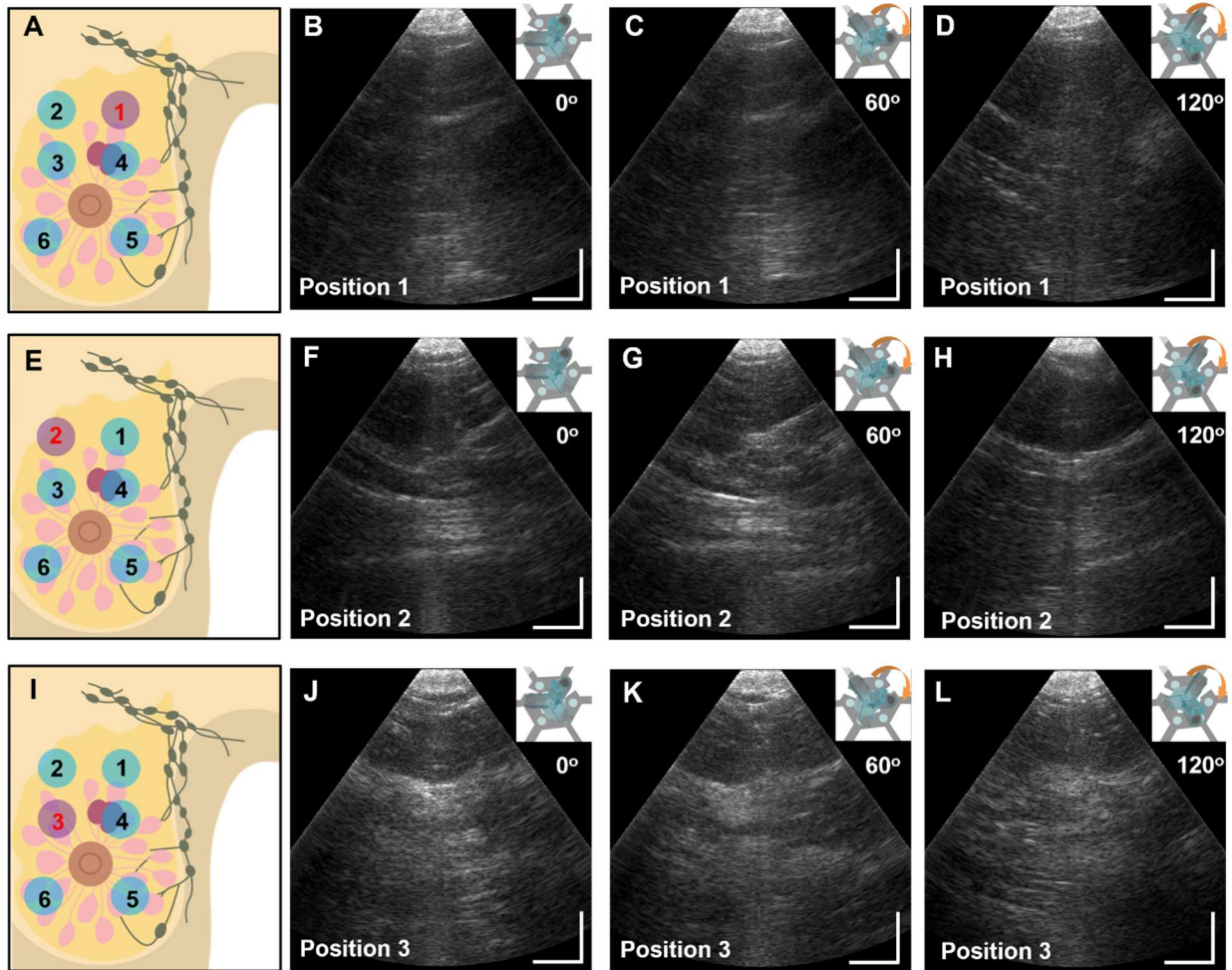
Figure 4.4. The imaging is under rotation and reconstruction at positions 1-3. (**A, E, I**) The schematic of the array rotation by the tracker. Ultrasound images by the array when it is rotated clockwise at different angles (0°, 60°, and 120°) at (**B-D**) Position 1, (**F-H**) Position 2, (**J-L**) Position 3.
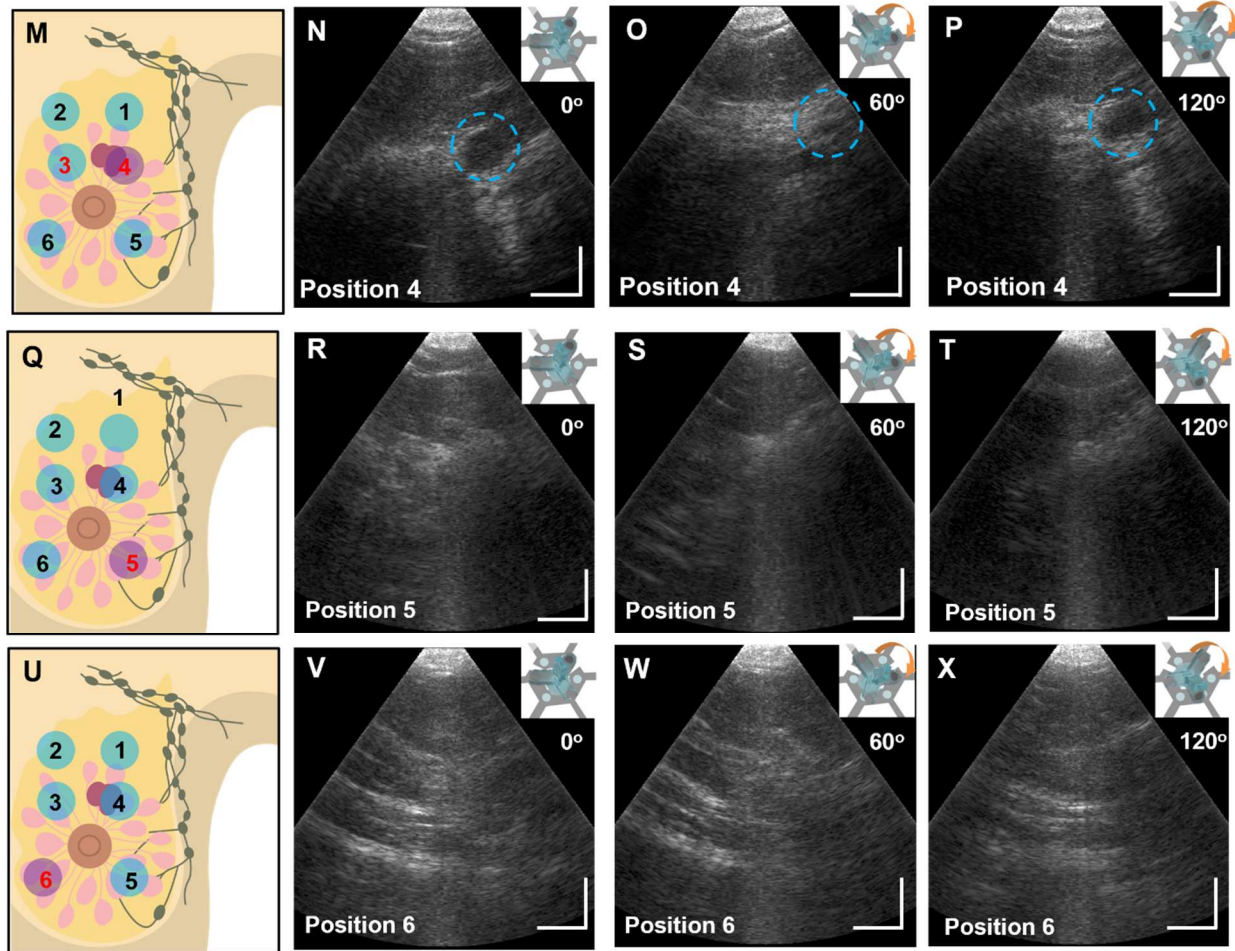
Fig. 4.5. The imaging under rotation and reconstruction at positions 4-6. (**M, Q, U**) The schematic of the array rotation by the tracker. Ultrasound images by the array when it is rotated clockwise at different angles (0º, 60º, and 120º) at (**N-P**) Position 1, (**R-T**) Position 2, (**V-U**) Position 3.

The cyst is identified as a roughly spherical shape via all three ultrasound images at various angles. The multi-angle reconstructed images and video based on the rotation images are shown in **Fig. 4.6**. We also used the same scanning sequence to examine the right breast of the subject (**Fig. 4.7**). A smaller cyst with a diameter of 0.3 cm was detected by the cUSBr-Patch in the right breast. Furthermore, after the cross-validation, we used the patch to check the imaging performance stability over time. The array can still detect the large cyst at Position 4 with similar

image quality after 30 minutes with 15-minute intervals (**Fig. 4.8**), indicating the repeatability of array positioning due to the honeycomb patch, a key capability to enable long-term monitoring.
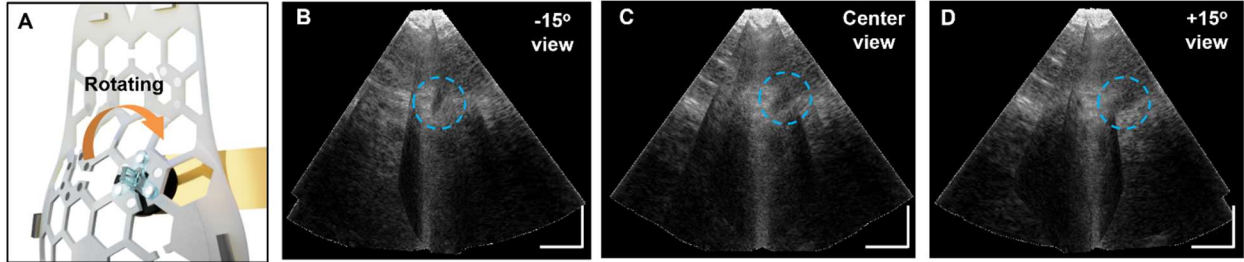
Figure. 4.6. The imaging reconstruction. (**A**) The schematic of the array rotation by the tracker. (**B-D**) Multi-angle image reconstruction at Position 4 with different view angles (-15°, center view, and +15°). The blue dashed circle indicates the hypoechoic lesion. Scale bar, 1 cm.
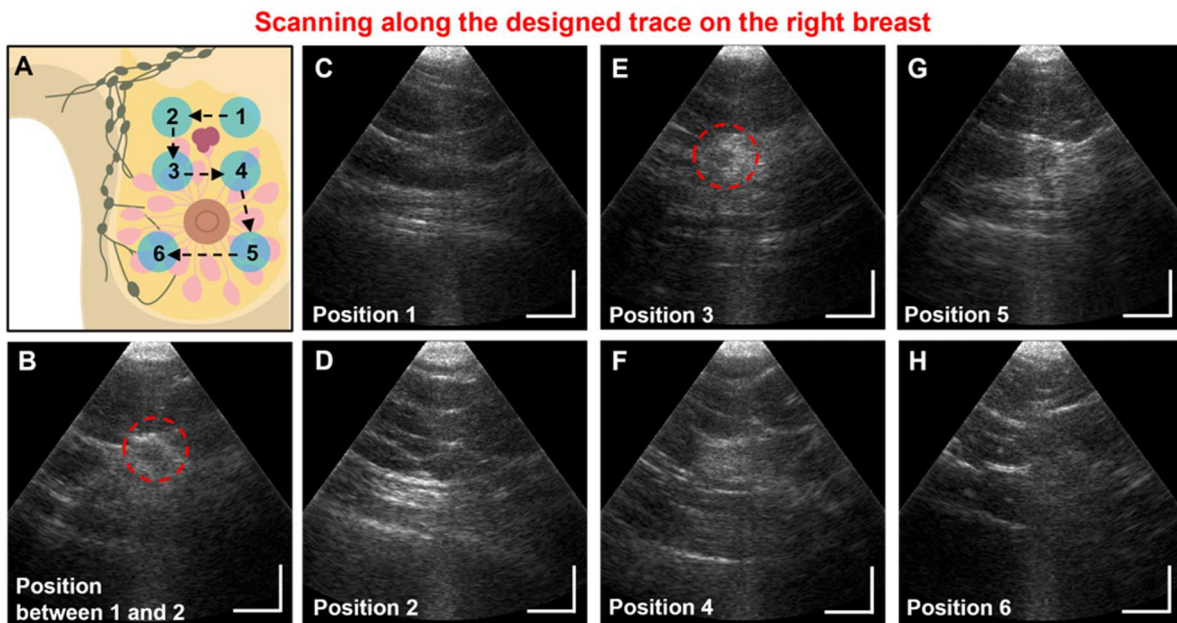
Figure 4.7. The cUSBr-Patch scans along the designed trace on the right breast. (**A**) The schematic of the right breast with the location of the cyst and the seven positions for imaging. (**B-F**) The photos of the cUSBr-Patch on the left breast of the subject at different positions. The red dashed circle indicates the cyst in the right breast. Scale bar, 1 cm.
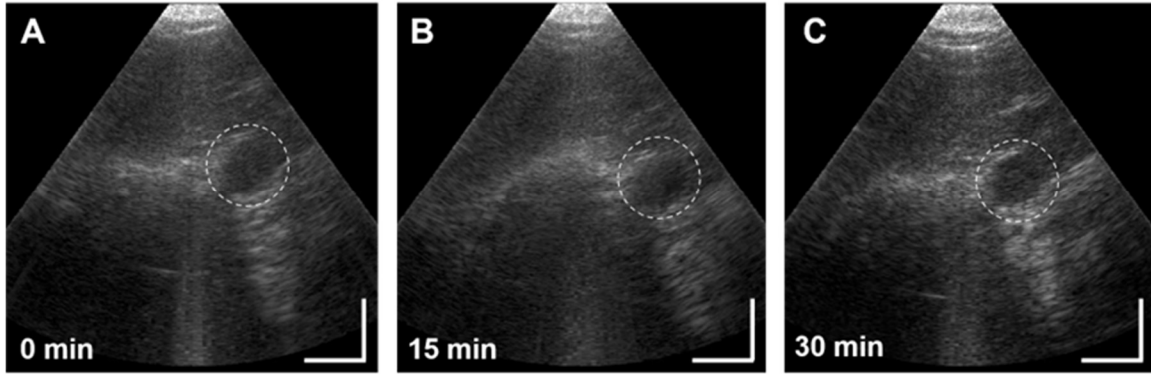
Figure 4.8. The reliability of the ultrasound imaging by the cUSBr-Patch. (**A**) Initial scanning. (**B**) The 2nd scan after 15 minutes. (**C**) The 3rd scan after 30 minutes. Scale bar, 1 cm.

4.2.2. Cross-validation with ML6-15 linear array

After finishing the examination on both breasts, we then used the GE ML6-15 linear array commercial probe with the setting at the same frequency (7 MHz) to cross-validate the imaging results by the cUSBr-Patch. The ultrasound specialist checked the same region on both breasts and found a larger cyst (diameter of 1 cm) in the left breast and a smaller cyst (diameter of 0.3 cm) in the right breast (**Fig. 4.9**), which indicates that our patch can precisely and observe these lesions and has the potential reliable capability to detect early-stage breast tumors. The cUSBr-Patch's ability to identify abnormalities on the order of 0.1 cm is essential for achieving early breast cancer detection well before tumors reach 2 cm in size [160].
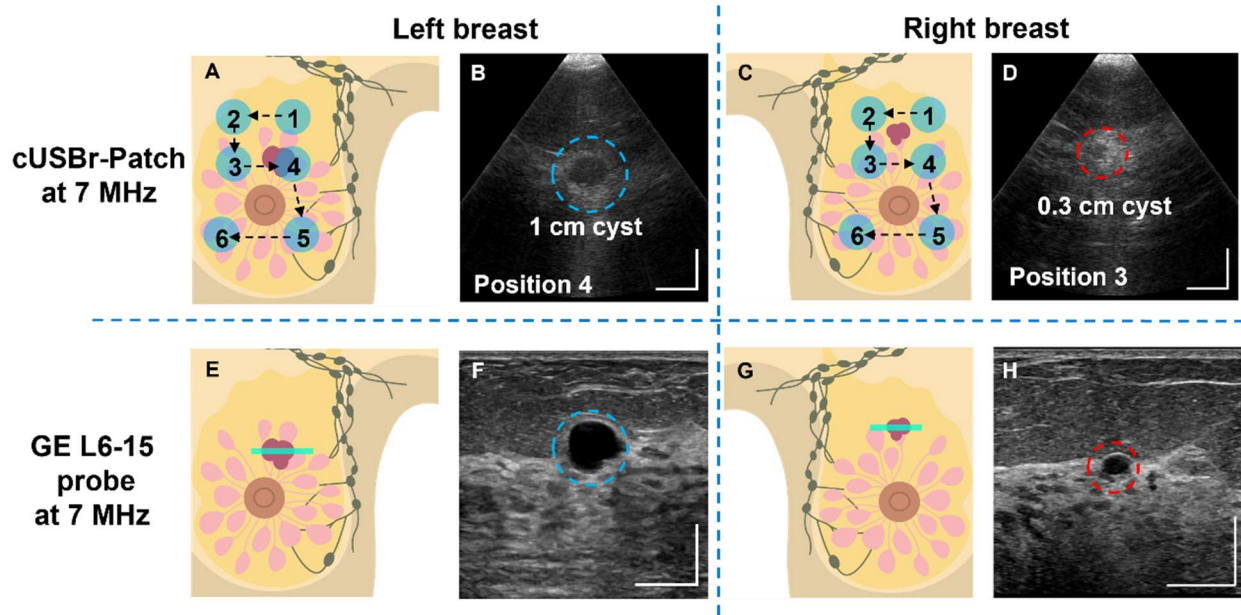
Figure 4.9. The cross-validation via GE Logiq E10 system with an ML6-15 linear array commercial probe. (**A**) The schematic of the left breast with the cyst. (**B**) The ultrasound image of the cyst in the left breast by the cUSBr-Patch. (**C**) The schematic of the right breast with the cyst. (**D**) The ultrasound image of the cyst on the right breast by the cUSBr-Patch. (**E**) The schematic of the left breast with the cyst and the scanning location of the ML6-15 probe. (**F**) The ultrasound image of the cyst in the left breast. (**G**) The schematic of the right breast with the cyst and the scanning location of the ML6-15 probe. (**H**) The ultrasound image of the cyst on the right breast. The teal line indicates the scanning position of the ML6-15 probe. The blue dashed circle and red dashed circle indicate different cysts in the left and right breast, respectively. Scale bar, 1 cm.

In addition, when we compare the field of view, this 1D phased array with a narrower aperture (8 mm in lateral dimension) provides the same field of view (fan shape with a 50 mm field of view at 3 cm depth) as the GE ML6-15 (**Fig. 4.10**). It also shows a great field of view at depths deeper than 30 mm. Although the phased array may not completely cover some shallow places close to the skin surface, this is still appropriate for deep lesions because the breast tumor has a very low probability near the skin and fat (within 10 mm depth) [161-163].
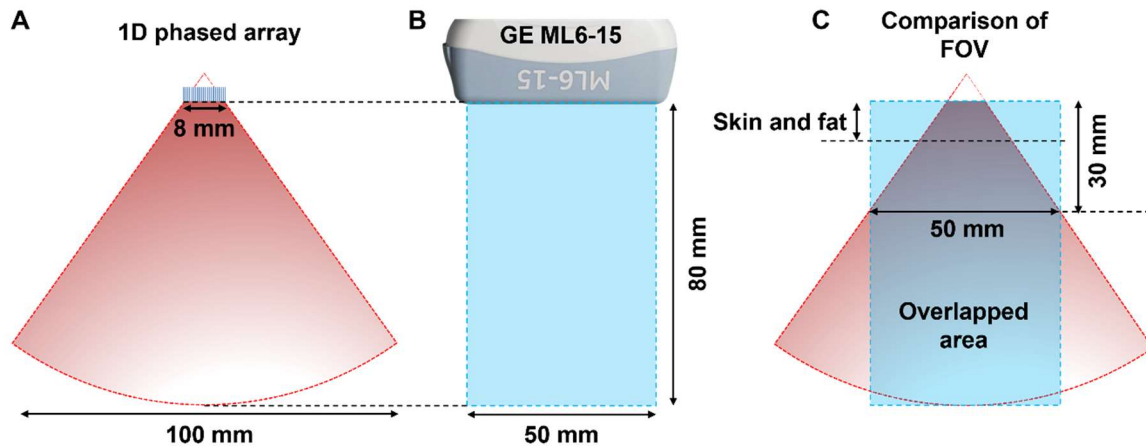
Figure 4.10. Comparison of the field of view between the 1D phased array and the GE ML6-15 linear probe. (**A**) The field of view of a 1D phased array with a depth of 80 mm (fig. S11). (**B**) The field of view of the GE ML6-15 linear probe (lateral dimension 50 mm and maximum depth 80 mm) [164]. (**C**) Comparison of the field of view. The phased array has a greater field of view at depths of approximately 30 mm or deeper.

In summary, we attempted to address the enormous challenge of imaging on the breast, which has the largest curvature on the human skin, in comparison to very recent designs that rely on hydrogels for fixed adhesion of the single ultrasound array [58] or the design based on a stretchable substrate with hundreds of elements for long-time imaging [146]. Either using a substrate with a large number of elements to completely cover the breast or frequently attaching/peeling a small patch at various locations on the breast is not a desirable strategy. Additionally, unlike heart, bladder, and other organ monitoring, breast imaging concentrates on the exact location of the cyst in the breast rather than requiring continuous imaging during a person's activities. This is the reason that we proposed the first-of-its-kind on-body ultrasound technology that used the combination of a conformable patch with a rotated phased array, to combine the advantages of HHUS and ABUS, especially for breast application. The cUSBr-Patch uses a nature-inspired honeycomb design to hold the array in place such that the array can be easily rotated and moved to different positions to

enable the observation of breast tissue in a more streamlined and standardized manner. The cUSBr-Patch additionally circumvents the need for a three-dimensional scanner or complex beamforming algorithm by using a high frequency phased array transducer with a fixed element pitch [146].

Chapter 5   Conclusions and Future Work

5.1   Conclusions

This study presents a novel ultrasound technology that is unique in its design, drawing inspiration from nature. It provides a non-invasive, wide field-of-view, real-time, user-friendly, and uninterrupted monitoring of curved breast tissue. Additionally, it is designed to be worn as a wearable device. This work employs a comprehensive system approach, encompassing the synthesis and characterization of a sophisticated piezoelectric crystal, the design and evaluation of an array, the development of a patch inspired by nature, and a clinical demonstration involving real-time imaging of the breast. The outcome is a novel device capable of non-invasively scanning and imaging soft tissues.

In this work, we obtained the following achievements:

1) The integration of a 1D array with a nature-inspired patch, along with the excellent electromechanical performance of the Yb/Bi PIN-PMN-PT crystal, enables high-performance image production. This system offers i) a deep image depth of approximately 80 mm, ii) sufficient contrast sensitivity of around 3 dB at a depth of 30 mm, iii) the desired axial/lateral resolution of 0.25/1.0 mm, and iv) a larger field of view for breast tissue imaging, which has been validated using a commercial ultrasound probe.

2) The honeycomb patch design, inspired by nature, offers several advancements. Firstly, it allows for easy scanning of 15 imaged sections, which helps in locating lesions outside of the usual four-quadrant designation. Secondly, it provides mechanical support and stability for the array, along with a tracker that enables imaging from different angles through rotation. Thirdly, it eliminates the need for the operator to constantly hold the device, which is crucial for hands-

free screening in home-based settings. Lastly, it ensures consistent and reliable breast tissue screening for long-term monitoring.

3) The cUSBr-Patch's capacity to clearly visualize cysts measuring approximately 0.3 cm in diameter renders it appropriate for early breast cancer screening. To capture images over a large area, users can reposition the array at various locations on the honeycomb-shaped patch. This allows them to obtain a comprehensive representation of the area. Meanwhile, hospitals can use multiple arrays simultaneously to achieve accurate imagery in terms of both space and time through multi-angle image reconstruction.

4) Additional benefits exist for practical applications, including the ability to reuse, the convenience of use, and improved practicality for continuous monitoring of breast abnormalities at home.

5.2   Future work

This study aimed to overcome the existing constraints of wearable ultrasound technologies, such as the ability to image large, curved organs and the use of advanced piezoelectric materials for ultrasonic arrays with enhanced performance. The advancement of ultrasound technology from being used at the bedside to being included in portable and wearable devices will enable its integration with big data collecting.

Future research will focus on several advancements, including the development of a patch that can be customized in size and has a polymer substrate. This patch will be embedded with multiple 1D arrays to eliminate the need for random manual scanning. Additionally, there will be extensive clinical trials that involve long-term imaging to monitor the effects of medical treatments or medication. Furthermore, a portable system with back-end capabilities will be developed to allow for daily self-screening. Consequently, the integration will facilitate the use of artificial

intelligence (AI) for diagnosis and the production of tailored ultrasonographic profiles. This capability enables the creation of personalized ultrasound profiles, as well as the collection of extensive data (such as tissue images and AI-analyzed outcomes), which may be promptly shared with medical professionals for rapid and unbiased evaluations. These systems can be designed to work together with wireless communication to continuously monitor various soft tissue conditions. The cUSBr-Patch measures image variations that can be predicted by changes over time in the progression of soft tissue abnormalities or as a response to medical treatment.

These advancements will allow for speedy and objective assessments. This progress is particularly significant in the context of breast cancer, as timely detection and evaluation of medical treatment responses are crucial for patient care.

References

[1] H. Wu, W. Gao, Z. Yin, Materials, Devices and Systems of Soft Bioelectronics for Precision Therapy, Advanced Healthcare Materials, 6 (2017) 1700017.

[2] X. Wang, Z. Liu, T. Zhang, Flexible Sensing Electronics for Wearable/Attachable Health Monitoring, Small, 13 (2017) 1602790.

[3] F. Tasnim, A. Sadraei, B. Datta, M. Khan, K.Y. Choi, A. Sahasrabudhe, T.A. Vega Gálvez, I. Wicaksono, O. Rosello, C. Nunez-Lopez, C. Dagdeviren, Towards personalized medicine: the evolution of imperceptible health-care technologies, Foresight, 20 (2018) 589-601.

[4] S.V. Fernandez, D. Sadat, F. Tasnim, D. Acosta, L. Schwendeman, S. Shahsavari, C. Dagdeviren, Ubiquitous conformable systems for imperceptible computing, foresight, ahead-of-print (2021).

[5] C. Dagdeviren, F. Javid, P. Joe, T. von Erlach, T. Bensel, Z. Wei, S. Saxton, C. Cleveland, L. Booth, S. McDonnell, J. Collins, A. Hayward, R. Langer, G. Traverso, Flexible piezoelectric devices for gastrointestinal motility sensing, Nature Biomedical Engineering, 1 (2017) 807-817.

[6] T. Sun, F. Tasnim, R.T. McIntosh, N. Amiri, D. Solav, M.T. Anbarani, D. Sadat, L. Zhang, Y. Gu, M.A. Karami, C. Dagdeviren, Decoding of facial strains via conformable piezoelectric interfaces, Nature Biomedical Engineering, 4 (2020) 954-972.

[7] I. Wicaksono, C.I. Tucker, T. Sun, C.A. Guerrero, C. Liu, W.M. Woo, E.J. Pence, C. Dagdeviren, A tailored, electronic textile conformable suit for large-scale spatiotemporal physiological sensing in vivo, npj Flexible Electronics, 4 (2020) 5.

[8] W. Zhang, L. You, X. Meng, B. Wang, D. Lin, Recent Advances on Conducting Polymers Based Nanogenerators for Energy Harvesting, Micromachines, 2021.

[9] C. Zhang, M.O.G. Nayeem, Z. Wang, X. Pu, C. Dagdeviren, Z.L. Wang, X. Zhang, R. Liu, Conductive hydrogels for bioenergy harvesting and self-powered application, Progress in Materials Science, 138 (2023) 101156.

[10] Z. Huang, Y. Hao, Y. Li, H. Hu, C. Wang, A. Nomoto, T. Pan, Y. Gu, Y. Chen, T. Zhang, W. Li, Y. Lei, N. Kim, C. Wang, L. Zhang, J.W. Ward, A. Maralani, X. Li, M.F. Durstock, A. Pisano, Y. Lin, S. Xu, Three-dimensional integrated stretchable electronics, Nature Electronics, 1 (2018) 473-480.

[11] C.M. Boutry, L. Beker, Y. Kaizawa, C. Vassos, H. Tran, A.C. Hinckley, R. Pfattner, S. Niu, J. Li, J. Claverie, Z. Wang, J. Chang, P.M. Fox, Z. Bao, Biodegradable and flexible arterial-pulse sensor for the wireless monitoring of blood flow, Nature Biomedical Engineering, 3 (2019) 47-57.

[12] G. Schwartz, B.C.K. Tee, J. Mei, A.L. Appleton, D.H. Kim, H. Wang, Z. Bao, Flexible polymer transistors with high pressure sensitivity for application in electronic skin and health monitoring, Nature Communications, 4 (2013) 1859.

[13] J. Kim, M. Lee, H.J. Shim, R. Ghaffari, H.R. Cho, D. Son, Y.H. Jung, M. Soh, C. Choi, S. Jung, K. Chu, D. Jeon, S.-T. Lee, J.H. Kim, S.H. Choi, T. Hyeon, D.-H. Kim, Stretchable silicon nanoribbon electronics for skin prosthesis, Nature Communications, 5 (2014).

[14] S. Hong, Y. Gu, J.K. Seo, J. Wang, P. Liu, Y.S. Meng, S. Xu, R. Chen, Wearable thermoelectrics for personalized thermoregulation, Science Advances, 5 (2019) eaaw0536.

[15] C. Dagdeviren, P. Joe, O.L. Tuzman, K.-I. Park, K.J. Lee, Y. Shi, Y. Huang, J.A. Rogers, Recent progress in flexible and stretchable piezoelectric devices for mechanical energy harvesting, sensing and actuation, Extreme Mechanics Letters, 9 (2016) 269-281.

[16] C. Dagdeviren, Z. Li, Z.L. Wang, Energy Harvesting from the Animal/Human Body for Self-Powered Electronics, Annual Review of Biomedical Engineering, 19 (2017) 85-108.

[17] C. Dagdeviren, Y. Shi, P. Joe, R. Ghaffari, G. Balooch, K. Usgaonkar, O. Gur, P.L. Tran, J.R. Crosby, M. Meyer, Y. Su, R. Chad Webb, A.S. Tedesco, M.J. Slepian, Y. Huang, J.A. Rogers, Conformal piezoelectric systems for clinical and experimental characterization of soft tissue biomechanics, Nature Materials, 14 (2015) 728.

[18] L. Persano, C. Dagdeviren, Y. Su, Y. Zhang, S. Girardo, D. Pisignano, Y. Huang, J.A. Rogers, High performance piezoelectric devices based on aligned arrays of nanofibers of poly(vinylidenefluoride-co-trifluoroethylene), Nature Communications, 4 (2013) 1633.

[19] C. Dagdeviren, Y. Su, P. Joe, R. Yona, Y. Liu, Y.-S. Kim, Y. Huang, A.R. Damadoran, J. Xia, L.W. Martin, Y. Huang, J.A. Rogers, Conformable amplified lead zirconate titanate sensors with enhanced piezoelectric response for cutaneous pressure monitoring, Nature Communications, 5 (2014) 4496.

[20] J.R. Windmiller, J. Wang, Wearable Electrochemical Sensors and Biosensors: A Review, Electroanalysis, 25 (2013) 29-46.

[21] X. Huang, Y. Liu, H. Cheng, W.-J. Shin, J.A. Fan, Z. Liu, C.-J. Lu, G.-W. Kong, K. Chen, D. Patnaik, S.-H. Lee, S. Hage-Ali, Y. Huang, J.A. Rogers, Materials and Designs for Wireless Epidermal Sensors of Hydration and Strain, Adv. Funct. Mater., (2014) 3846–3854.

[22] H.J. Chung, M.S. Sulkin, J.S. Kim, C. Goudeseune, H.Y. Chao, J.W. Song, S.Y. Yang, Y.Y. Hsu, R. Ghaffari, I.R. Efimov, J.A. Rogers, Stretchable, Multiplexed pH Sensors With Demonstrations on Rabbit and Human Hearts Undergoing Ischemia, Advanced Healthcare Materials, 3 (2014) 59-68.

[23] M.T. Ghoneim, A. Nguyen, N. Dereje, J. Huang, G.C. Moore, P.J. Murzynowski, C. Dagdeviren, Recent Progress in Electrochemical pH-Sensing Materials and Configurations for Biomedical Applications, Chemical Reviews, 119 (2019) 5248-5297.

[24] W. Gao, S. Emaminejad, H.Y.Y. Nyein, S. Challa, K. Chen, A. Peck, H.M. Fahad, H. Ota, H. Shiraki, D. Kiriya, D.-H. Lien, G.A. Brooks, R.W. Davis, A. Javey, Fully integrated wearable sensor arrays for multiplexed in situ perspiration analysis, Nature, 529 (2016) 509-514.

[25] G.S. Jeong, D.-H. Baek, H.C. Jung, J.H. Song, J.H. Moon, S.W. Hong, I.Y. Kim, S.-H. Lee, 2Solderable and electroplatable flexible electronic circuit on a porous stretchable elastomer, Nature Communications, 3 (2012) 977.

[26] C. Wang, C. Wang, Z. Huang, S. Xu, Materials and Structures toward Soft Electronics, Advanced Materials, 30 (2018) 1801368.

[27] S.V. Fernandez, F. Cai, S. Chen, E. Suh, J. Tiepelt, R. McIntosh, C. Marcus, D. Acosta, D. Mejorado, C. Dagdeviren, On-Body Piezoelectric Energy Harvesters through Innovative Designs and Conformable Structures, ACS Biomaterials Science & Engineering, (2021).

[28] S.V. Fernandez, D. Sadat, F. Tasnim, D. Acosta, L. Schwendeman, S. Shahsavari, C. Dagdeviren, Ubiquitous conformable systems for imperceptible computing, foresight, 24 (2022) 75-98.

[29] X. Meng, Z. Zhang, D. Lin, W. Liu, S. Zhou, S. Ge, Y. Su, C. Peng, L. Zhang, Effects of particle size of dielectric fillers on the output performance of piezoelectric and triboelectric nanogenerators, Journal of Advanced Ceramics, 10 (2021) 991-1000.

[30] Y. Du, W. Du, D. Lin, M. Ai, S. Li, L. Zhang, Recent Progress on Hydrogel-Based Piezoelectric Devices for Biomedical Applications, Micromachines, 2023.

[31] Y. Zhuang, J. Li, Q. Hu, S. Han, W. Liu, C. Peng, Z. Li, L. Zhang, X. Wei, Z. Xu, Flexible composites with Ce-doped BaTiO3/P(VDF-TrFE) nanofibers for piezoelectric device, Composites Science and Technology, 200 (2020) 108386.

[32] C. Wang, C. Wang, Z. Huang, S. Xu, Materials and Structures toward Soft Electronics, Advanced Materials, 30 (2018) 1801368.

[33] M.T. Chorsi, E.J. Curry, H.T. Chorsi, R. Das, J. Baroody, P.K. Purohit, H. Ilies, T.D. Nguyen, Piezoelectric Biomaterials for Sensors and Actuators, Advanced Materials, 31 (2019) 1802084.

[34] J. Briscoe, S. Dunn, Piezoelectric nanogenerators – a review of nanostructured piezoelectric energy harvesters, Nano Energy, 14 (2015) 15-29.

[35] F. Narita, M. Fox, A Review on Piezoelectric, Magnetostrictive, and Magnetoelectric Materials and Device Technologies for Energy Harvesting Applications, Advanced Engineering Materials, 20 (2018) 1700743.

[36] Z. Yang, S. Zhou, J. Zu, D. Inman, High-Performance Piezoelectric Energy Harvesters and Their Applications, Joule, 2 (2018) 642-697.

[37] L. Jiaqing, T. Guo, Y. Weiqing, D. Weili, Recent progress in flexible piezoelectric devices toward human-machine interactions, Recent progress in flexible piezoelectric devices toward human-machine interactions, 2 (2022) 22.

[38] N. Amiri, F. Tasnim, M. Tavakkoli Anbarani, C. Dagdeviren, M.A. Karami, Experimentally verified finite element modeling and analysis of a conformable piezoelectric sensor, Smart Materials and Structures, 30 (2021) 085017.

[39] Y. Guan, L. Tu, K. Ren, X. Kang, Y. Tian, W. Deng, P. Yu, C. Ning, R. Fu, G. Tan, L. Zhou, Soft, Super-Elastic, All-Polymer Piezoelectric Elastomer for Artificial Electronic Skin, ACS Applied Materials & Interfaces, 15 (2023) 1736-1747.

[40] C. Dagdeviren, B.D. Yang, Y. Su, P.L. Tran, P. Joe, E. Anderson, J. Xia, V. Doraiswamy, B. Dehdashti, X. Feng, B. Lu, R. Poston, Z. Khalpey, R. Ghaffari, Y. Huang, M.J. Slepian, J.A. Rogers, Conformal piezoelectric energy harvesting and storage from motions of the heart, lung, and diaphragm, Proceedings of the National Academy of Sciences, 111 (2014) 1927.

[41] M.O.G. Nayeem, S. Lee, H. Jin, N. Matsuhisa, H. Jinno, A. Miyamoto, T. Yokota, T. Someya, All-nanofiber–based, ultrasensitive, gas-permeable mechanoacoustic sensors for

continuous long-term heart monitoring, Proceedings of the National Academy of Sciences, 117 (2020) 7063-7070.

[42] S. Chun, J.-S. Kim, Y. Yoo, Y. Choi, S.J. Jung, D. Jang, G. Lee, K.-I. Song, K.S. Nam, I. Youn, D. Son, C. Pang, Y. Jeong, H. Jung, Y.-J. Kim, B.-D. Choi, J. Kim, S.-P. Kim, W. Park, S. Park, An artificial neural tactile sensing system, Nature Electronics, 4 (2021) 429-438.

[43] C. Wang, X. Li, H. Hu, L. Zhang, Z. Huang, M. Lin, Z. Zhang, Z. Yin, B. Huang, H. Gong, S. Bhaskaran, Y. Gu, M. Makihata, Y. Guo, Y. Lei, Y. Chen, C. Wang, Y. Li, T. Zhang, Z. Chen, A.P. Pisano, L. Zhang, Q. Zhou, S. Xu, Monitoring of the central blood pressure waveform via a conformal ultrasonic device, Nature Biomedical Engineering, 2 (2018) 687-695.

[44] F. Wang, P. Jin, Y. Feng, J. Fu, P. Wang, X. Liu, Y. Zhang, Y. Ma, Y. Yang, A. Yang, X. Feng, Flexible Doppler ultrasound device for the monitoring of blood flow velocity, Science Advances, 7 (2021) eabi9283.

[45] A. Barone, Generation, Detection and Measurement of Ultrasound, in: R.W. Leonard, A. Barone, R. Truell, C. Elbaum, B.E. Noltingk (Eds.) Akustik II / Acoustics II, Springer Berlin Heidelberg, Place Published, 1962, pp. 74-152.

[46] Q. Zhou, S. Lau, D. Wu, K. Kirk Shung, Piezoelectric films for high frequency ultrasonic transducers in biomedical applications, Progress in Materials Science, 56 (2011) 139-174.

[47] Q. Zhou, K.H. Lam, H. Zheng, W. Qiu, K.K. Shung, Piezoelectric single crystal ultrasonic transducers for biomedical applications, Progress in Materials Science, 66 (2014) 87-111.

[48] C.M.W. Daft, Conformable transducers for large-volume, operator-independent imaging, 2010 IEEE International Ultrasonics Symposium, 2010, pp. 798-808.

[49] L. Zhang, W. Du, J.-H. Kim, C.-C. Yu, C. Dagdeviren, An Emerging Era: Conformable Ultrasound Electronics, Advanced Materials, 36 (2023) 2307664.

[50] R.S. Singh, M.O. Culjat, S.P. Vampola, K. Williams, Z.D. Taylor, H. Lee, W.S. Grundfest, E.R. Brown, P3D-6 Simulation, Fabrication, and Characterization of a Novel Flexible, Conformal Ultrasound Transducer Array, 2007 IEEE Ultrasonics Symposium Proceedings, 2007, pp. 1824-1827.

[51] M. Lin, H. Hu, S. Zhou, S. Xu, Soft wearable devices for deep-tissue sensing, Nature Reviews Materials, 7 (2022) 850-869.

[52] J. Li, Y. Ma, T. Zhang, K.K. Shung, B. Zhu, Recent Advancements in Ultrasound Transducer: From Material Strategies to Biomedical Applications, BME Frontiers, 2022 (2022) 9764501.

[53] L. Jiang, J. Wu, Emerging ultrasonic bioelectronics for personalized healthcare, Progress in Materials Science, 136 (2023) 101110.

[54] D. Ren, Y. Yin, C. Li, R. Chen, J. Shi, Recent Advances in Flexible Ultrasonic Transducers: From Materials Optimization to Imaging Applications, Micromachines, 14 (2023) 126.

[55] L. Jiang, Y. Yang, Y. Chen, Q. Zhou, Ultrasound-induced wireless energy harvesting: From materials strategies to functional applications, Nano Energy, 77 (2020) 105131.

[56] H. Hu, X. Zhu, C. Wang, L. Zhang, X. Li, S. Lee, Z. Huang, R. Chen, Z. Chen, C. Wang, Y. Gu, Y. Chen, Y. Lei, T. Zhang, N. Kim, Y. Guo, Y. Teng, W. Zhou, Y. Li, A. Nomoto, S. Sternini, Q. Zhou, M. Pharr, F.L. di Scalea, S. Xu, Stretchable ultrasonic transducer arrays for three-dimensional imaging on complex surfaces, Science Advances, 4 (2018) eaar3979.

[57] X. Sun, A.J. Croxford, B.W. Drinkwater, Continuous monitoring with a permanently installed high-resolution ultrasonic phased array, Structural Health Monitoring, (2023) 14759217231152413.

[58] C. Wang, X. Chen, L. Wang, M. Makihata, H.-C. Liu, T. Zhou, X. Zhao, Bioadhesive ultrasound for long-term continuous imaging of diverse organs, Science, 377 (2022) 517-523.

[59] M. Lin, Z. Zhang, X. Gao, Y. Bian, R.S. Wu, G. Park, Z. Lou, Z. Zhang, X. Xu, X. Chen, A. Kang, X. Yang, W. Yue, L. Yin, C. Wang, B. Qi, S. Zhou, H. Hu, H. Huang, M. Li, Y. Gu, J. Mu, A. Yang, A. Yaghi, Y. Chen, Y. Lei, C. Lu, R. Wang, J. Wang, S. Xiang, E.B. Kistler, N. Vasconcelos, S. Xu, A fully integrated wearable ultrasound system to monitor deep tissues in moving subjects, Nature Biotechnology, (2023).

[60] W. Du, L. Zhang, E. Suh, D. Lin, C. Marcus, L. Ozkan, A. Ahuja, S. Fernandez, I.I. Shuvo, D. Sadat, W. Liu, F. Li, A.P. Chandrakasan, T. Ozmen, C. Dagdeviren, Conformable ultrasound breast patch for deep tissue scanning and imaging, Science Advances, 9 (2023) eadh5325.

[61] L. Zhang, C. Marcus, D. Lin, D. Mejorado, S.J. Schoen, T.T. Pierce, V. Kumar, S.V. Fernandez, D. Hunt, Q. Li, I.I. Shuvo, D. Sadat, W. Du, H. Edenbaum, L. Jin, W. Liu, Y.C.

Eldar, F. Li, A.P. Chandrakasan, A.E. Samir, C. Dagdeviren, A conformable phased-array ultrasound patch for bladder volume monitoring, Nature Electronics, 7 (2024) 77-90.

[62] C. Wang, B. Qi, M. Lin, Z. Zhang, M. Makihata, B. Liu, S. Zhou, Y.-h. Huang, H. Hu, Y. Gu, Y. Chen, Y. Lei, T. Lee, S. Chien, K.-I. Jang, E.B. Kistler, S. Xu, Continuous monitoring of deep-tissue haemodynamics with stretchable ultrasonic phased arrays, Nature Biomedical Engineering, 5 (2021) 749-758.

[63] P. Jin, J. Fu, F. Wang, Y. Zhang, P. Wang, X. Liu, Y. Jiao, H. Li, Y. Chen, Y. Ma, X. Feng, A flexible, stretchable system for simultaneous acoustic energy transfer and communication, Science Advances, 7 (2021) eabg2507.

[64] L. Jiang, G. Lu, Y. Yang, Y. Xu, F. Qi, J. Li, B. Zhu, Y. Chen, Multichannel Piezo-Ultrasound Implant with Hybrid Waterborne Acoustic Metastructure for Selective Wireless Energy Transfer at Megahertz Frequencies, Advanced Materials, 33 (2021) 2104251.

[65] X. Meng, X. Xiao, S. Jeon, D. Kim, B.-J. Park, Y.-J. Kim, N. Rubab, S. Kim, S.-W. Kim, An Ultrasound-Driven Bioadhesive Triboelectric Nanogenerator for Instant Wound Sealing and Electrically Accelerated Healing in Emergencies, Advanced Materials, 35 (2023) 2209054.

[66] W. Lyu, Y. Ma, S. Chen, H. Li, P. Wang, Y. Chen, X. Feng, Flexible Ultrasonic Patch for Accelerating Chronic Wound Healing, Advanced Healthcare Materials, 10 (2021) 2100785.

[67] L. Jiang, G. Lu, Y. Zeng, Y. Sun, H. Kang, J. Burford, C. Gong, M.S. Humayun, Y. Chen, Q. Zhou, Flexible ultrasound-induced retinal stimulating piezo-arrays for biomimetic visual prostheses, Nature Communications, 13 (2022) 3853.

[68] X. Wan, P. Chen, Z. Xu, X. Mo, H. Jin, W. Yang, S. Wang, J. Duan, B. Hu, Z. Luo, L. Huang, J. Zhou, Hybrid-Piezoelectret Based Highly Efficient Ultrasonic Energy Harvester for Implantable Electronics, Advanced Functional Materials, 32 (2022) 2200589.

[69] T. Zhang, H. Liang, Z. Wang, C. Qiu, Y.B. Peng, X. Zhu, J. Li, X. Ge, J. Xu, X. Huang, J. Tong, J. Ou-Yang, X. Yang, F. Li, B. Zhu, Piezoelectric ultrasound energy–harvesting device for deep brain stimulation and analgesia applications, Science Advances, 8 (2022) eabk0159.

[70] S. Li, J. Xu, R. Li, Y. Wang, M. Zhang, J. Li, S. Yin, G. Liu, L. Zhang, B. Li, Q. Gu, Y. Su, Stretchable Electronic Facial Masks for Sonophoresis, ACS Nano, 16 (2022) 5961-5974.

[71] C.-C. Yu, A. Shah, N. Amiri, C. Marcus, M.O.G. Nayeem, A.K. Bhayadia, A. Karami, C. Dagdeviren, A Conformable Ultrasound Patch for Cavitation-Enhanced Transdermal Cosmeceutical Delivery, Advanced Materials, 35 (2023) 2300066.

[72] S. Łukasiewicz, M. Czeczelewski, A. Forma, J. Baj, R. Sitarz, A. Stanisławek, Breast Cancer—Epidemiology, Risk Factors, Classification, Prognostic Markers, and Current Treatment Strategies—An Updated Review, Cancers, 13 (2021) 4287.

[73] S.A. Narod, J. Iqbal, A.B. Miller, Why have breast cancer mortality rates declined?, Journal of Cancer Policy, 5 (2015) 8-17.

[74] K.C. Oeffinger, E.T. Fontham, R. Etzioni, Breast cancer screening for women at average risk: 2015 guideline update from the American Cancer Society, JAMA, 314 (2015) 1599.

[75] L.N. Shulman, W. Willett, A. Sievers, F.M. Knaul, Breast Cancer in Developing Countries: Opportunities for Improved Survival, Journal of Oncology, 2010 (2010).

[76] G. Cserni, E. Chmielik, B. Cserni, T. Tot, The new TNM-based staging of breast cancer, Virchows Archiv, 472 (2018) 697-703.

[77] https://www.breastcancer.org/pathology-report/breast-cancer-stages.

[78] https://www.cancer.org/cancer/types/breast-cancer/understanding-a-breast-cancer-diagnosis.html.

[79] M. Cianfrocca, L.J. Goldstein, Prognostic and Predictive Factors in Early-Stage Breast Cancer, The Oncologist, 9 (2004) 606-616.

[80] L.K. D. Mulholland MW, Doherty GM, Upchurch Jr GR, Alam H, Pawlik TM., Greenfield's Surgery: Scientific Principles & Practice, Philadelphia Wolters Klewer, Place Published, 2017.

[81] V.Y. Sohn, A.Z. Fau, J.A. Sebesta, S.J. Fau, T.A. Brown, T.A. Brown, Primary tumor location impacts breast cancer survival, The American Journal of Surgery, 195 (2008) 641-644.

[82] Z.S. Lima, M.R. Ebadi, G. Amjad, L. Younesi, Application of Imaging Technologies in Breast Cancer Detection: A Review Article, Open Access Maced J Med Sci., 7 (2019) 838-848.

[83] C.K. Kuhl, S. Schrading, C.C. Leutner, N. Morakkabati-Spitz, E. Wardelmann, R. Fimmers, W. Kuhn, H.H. Schild, Mammography, Breast Ultrasound, and Magnetic Resonance

Imaging for Surveillance of Women at High Familial Risk for Breast Cancer, Journal of Clinical Oncology, 23 (2005) 8469-8476.

[84] T.M. Kolb, J. Lichy, J.H. Newhouse, Comparison of the Performance of Screening Mammography, Physical Examination, and Breast US and Evaluation of Factors that Influence Them: An Analysis of 27,825 Patient Evaluations, Radiology, 225 (2002) 165-175.

[85] H.J. Shin, H.H. Kim, J.H. Cha, Current status of automated breast ultrasonography, Ultrasonography, 34 (2015) 165-172.

[86] M. Zanotel, I. Bednarova, V. Londero, A. Linda, M. Lorenzon, R. Girometti, C. Zuiani, Automated breast ultrasound: basic principles and emerging clinical applications, La radiologia medica, 123 (2018) 1-12.

[87] R. Rella, P. Belli, M. Giuliani, E. Bufi, G. Carlino, P. Rinaldi, R. Manfredi, Automated Breast Ultrasonography (ABUS) in the Screening and Diagnostic Setting: Indications and Practical Use, Academic Radiology, 25 (2018) 1457-1470.

[88] K. Kratkiewicz, A. Pattyn, N. Alijabbari, M. Mehrmohammadi, Ultrasound and Photoacoustic Imaging of Breast Cancer: Clinical Systems, Challenges, and Future Outlook, Journal of Clinical Medicine, 11 (2022) 1165.

[89] C.-Y. Lee, T.-L. Truong, P.-C. Li, Automated Conformal Ultrasound Scanning for Breast Screening, Journal of Medical and Biological Engineering, 38 (2018) 116-128.

[90] S. Zhang, F. Li, High performance ferroelectric relaxor-PbTiO3 single crystals: Status and perspective, Journal of Applied Physics, 111 (2012) 031301.

[91] S. Zhang, F. Li, X. Jiang, J. Kim, J. Luo, X. Geng, Advantages and challenges of relaxor-PbTiO3 ferroelectric crystals for electroacoustic transducers – A review, Progress in Materials Science, 68 (2015) 1-66.

[92] T. Zheng, J. Wu, D. Xiao, J. Zhu, Recent development in lead-free perovskite piezoelectric bulk materials, Progress in Materials Science, 98 (2018) 552-624.

[93] X. Gao, J. Yang, J. Wu, X. Xin, Z. Li, X. Yuan, X. Shen, S. Dong, Piezoelectric Actuators and Motors: Materials, Designs, and Applications, Advanced Materials Technologies, 5 (2020) 1900716.

[94] H. Jin, X. Gao, K. Ren, J. Liu, L. Qiao, M. Liu, W. Chen, Y. He, S. Dong, Z. Xu, F. Li, Review on Piezoelectric Actuators Based on High-Performance Piezoelectric Materials,

IEEE Transactions on Ultrasonics, Ferroelectrics, and Frequency Control, 69 (2022) 3057-3069.

[95] A.V. Hippel, Dielectric Materials and Applications, Technology Press of MIT, Place Published, 1954.

[96] K.C. Kao, Dielectric Phenomena in Solids, Elsevier Academic Press, Place Published, 2004.

[97] S. Jiang, L. Jin, H. Hou, L. Zhang, Chapter 8 - Polymer-Based Nanocomposites with High Dielectric Permittivity, in: K. Song, C. Liu, J.Z. Guo (Eds.) Polymer-Based Multifunctional Nanocomposites and Their Applications, Elsevier, Place Published, 2019, pp. 201-243.

[98] C.J. Dias, D.K. Das-Gupta, Ferroelectric Polymer and Ceramic-Polymer Composites, Trans Tech Publications Ltd., Place Published, 1994.

[99] J.H. Lee, S. Zhang, Y. Bar-Cohen, S. Sherrit, High Temperature, High Power Piezoelectric Composite Transducers, Sensors, 14 (2014).

[100] L. Jin, V. Porokhonskyy, D. Damjanovic, Domain wall contributions in Pb(Zr,Ti)O3 ceramics at morphotropic phase boundary: A study of dielectric dispersion, Applied Physics Letters, 96 (2010) 242902.

[101] T.F. de Oliveira, C.N. Pai, M.Y. Matuda, J.C. Adamowski, F. Buiochi, Development of a 2.25 MHz flexible array ultrasonic transducer, Research on Biomedical Engineering, 35 (2019) 27-37.

[102] T. Kim, Z. Cui, W. Chang, H. Kim, Y. Zhu, X. Jiang, Flexible 1-3 Composite Ultrasound Transducers with Silver Nanowire-based Stretchable Electrodes, IEEE Transactions on Industrial Electronics, (2019) 1-1.

[103] V. Pashaei, P. Dehghanzadeh, G. Enwia, M. Bayat, S.J.A. Majerus, S. Mandal, Flexible Body-Conformal Ultrasound Patches for Image-Guided Neuromodulation, IEEE Transactions on Biomedical Circuits and Systems, 14 (2020) 305-318.

[104] S. Sadeghpour, B. Lips, M. Kraft, R. Puers, Bendable Piezoelectric Micromachined Ultrasound Transducer (PMUT) Arrays Based on Silicon-On-Insulator (SOI) Technology, Journal of Microelectromechanical Systems, (2020) 1-9.

[105] W. Liu, W. Chen, C. Zhu, D. Wu, Design and micromachining of a stretchable two-dimensional ultrasonic array, Micro and Nano Engineering, 13 (2021) 100096.

[106] Q. Zhang, T. Ma, C. Wang, X. Liu, Y. Li, Y. Chang, J. Liu, J. Huang, Y. Xiao, T. Pan, H. Zheng, Transformable Ultrasonic Array Transducer for Multiscale Imaging and Beamforming, IEEE Transactions on Industrial Electronics, 69 (2022) 3078-3087.

[107] T.R. Shrout, S.J. Zhang, Lead-free piezoelectric ceramics: Alternatives for PZT?, Journal of Electroceramics, 19 (2007) 113-126.

[108] S. Trolier-McKinstry, S. Zhang, A.J. Bell, X. Tan, High-Performance Piezoelectric Crystals, Ceramics, and Films, Annual Review of Materials Research, 48 (2018) 191-217.

[109] L. Zhang, Z. Xu, Y. Feng, Y. Hu, X. Yao, Synthesis, sintering and characterization of PNZST ceramics from high-energy ball milling process, Ceramics International, 34 (2008) 709-713.

[110] D. Lin, Z. Li, F. Li, Z. Xu, X. Yao, Characterization and piezoelectric thermal stability of PIN–PMN–PT ternary ceramics near the morphotropic phase boundary, Journal of Alloys and Compounds, 489 (2010) 115-118.

[111] K.K. Shung, J.M. Cannata, Q.F. Zhou, Piezoelectric materials for high frequency medical imaging applications: A review, Journal of Electroceramics, 19 (2007) 141-147.

[112] F. Li, D. Lin, Z. Chen, Z. Cheng, J. Wang, C. Li, Z. Xu, Q. Huang, X. Liao, L.-Q. Chen, T.R. Shrout, S. Zhang, Ultrahigh piezoelectricity in ferroelectric ceramics by design, Nature Materials, 17 (2018) 349-354.

[113] C. Li, B. Xu, D. Lin, S. Zhang, L. Bellaiche, T.R. Shrout, F. Li, Atomic-scale origin of ultrahigh piezoelectricity in samarium-doped PMN-PT ceramics, Physical Review B, 101 (2020) 140102.

[114] Z. Zhang, M. Su, F. Li, R. Liu, R. Cai, G. Li, Q. Jiang, H. Zhong, T.R. Shrout, S. Zhang, H. Zheng, W. Qiu, New Sm-PMN-PT Ceramic-Based 2-D Array for Low-Intensity Ultrasound Therapy Application, IEEE Transactions on Ultrasonics, Ferroelectrics, and Frequency Control, 67 (2020) 2085-2094.

[115] Z. Zhang, F. Li, R. Chen, T. Zhang, X. Cao, S. Zhang, T.R. Shrout, H. Zheng, K.K. Shung, M.S. Humayun, W. Qiu, Q. Zhou, High-Performance Ultrasound Needle Transducer Based on Modified PMN-PT Ceramic With Ultrahigh Clamped Dielectric Permittivity, IEEE Transactions on Ultrasonics, Ferroelectrics, and Frequency Control, 65 (2018) 223-230.

[116] E. Buixaderas, D. Nuzhnyy, J. Petzelt, L. Jin, D. Damjanovic, Polar lattice vibrations and phase transition dynamics in $Pb(Zr_{1-x}Ti_x)O_3$, Physical Review B, 84 (2011) 184302.

[117] E. Buixaderas, I. Gregora, M. Savinov, J. Hlinka, L. Jin, D. Damjanovic, B. Malic, Compositional behavior of Raman-active phonons in $Pb(Zr_{1-x}Ti_x)O_3$ ceramics, Physical Review B, 91 (2015) 014104.

[118] Y. Yamashita, T. Karaki, H.Y. Lee, H. Wan, H.P. Kim, X. Jiang, A Review of Lead Perovskite Piezoelectric Single Crystals and Their Medical Transducers Application, IEEE Transactions on Ultrasonics, Ferroelectrics, and Frequency Control, 69 (2022) 3048-3056.

[119] D. Damjanovic, N. Klein, J.I.N. Li, V. Porokhonskyy, What can be expected from lead-free piezoelectric materials? Functional Materials Letters, 03 (2010) 5-13.

[120] Z. Zhang, J. Xu, L. Yang, S. Liu, J. Xiao, X. Li, X.a. Wang, H. Luo, Design and comparison of PMN-PT single crystals and PZT ceramics based medical phased array ultrasonic transducer, Sensors and Actuators A: Physical, 283 (2018) 273-281.

[121] C.-M. Wong, Y. Chen, H. Luo, J. Dai, K.-H. Lam, H.L.-w. Chan, Development of a 20-MHz wide-bandwidth PMN-PT single crystal phased-array ultrasound transducer, Ultrasonics, 73 (2017) 181-186.

[122] F. Li, M.J. Cabral, B. Xu, Z. Cheng, E.C. Dickey, J.M. LeBeau, J. Wang, J. Luo, S. Taylor, W. Hackenberger, L. Bellaiche, Z. Xu, L.-Q. Chen, T.R. Shrout, S. Zhang, Giant piezoelectricity of Sm-doped $Pb(Mg_{1/3}Nb_{2/3})O_3$-$PbTiO_3$ single crystals, Science, 364 (2019) 264-268.

[123] Q. Li, Y. Liu, J. Liu, K. Song, H. Guo, F. Li, Z. Xu, Enhanced Piezoelectric Properties and Improved Property Uniformity in Nd-Doped PMN-PT Relaxor Ferroelectric Single Crystals, Advanced Functional Materials, 32 (2022) 2201719.

[124] Y. Liu, Q. Li, L. Qiao, Z. Xu, F. Li, Achieving Giant Piezoelectricity and High Property Uniformity Simultaneously in a Relaxor Ferroelectric Crystal through Rare-Earth Element Doping, Advanced Science, 9 (2022) 2204631.

[125] L. Yang, H. Huang, Z. Xi, L. Zheng, S. Xu, G. Tian, Y. Zhai, F. Guo, L. Kong, Y. Wang, W. Lü, L. Yuan, M. Zhao, H. Zheng, G. Liu, Simultaneously achieving giant piezoelectricity and record coercive field enhancement in relaxor-based ferroelectric crystals, Nature Communications, 13 (2022) 2444.

[126] C.M. Sayers, C.E. Tait, Ultrasonic properties of transducer backings, Ultrasonics, 22 (1984) 57-60.

[127] [127] H. Kim, J. Yoo, D. Heo, Y.S. Seo, H.G. Lim, H.H. Kim, High-Attenuation Backing Layer for Miniaturized Ultrasound Imaging Transducer, IEEE Transactions on Ultrasonics, Ferroelectrics, and Frequency Control, 69 (2022) 1960-1969.

[128] [128] A. Amry Amin, I. Mohamad Pauzi, S. Suhairy, A. Mohd Noorul Ikhsan, Effect of backing layer composition on ultrasonic probe bandwidth, RnD Seminar 2010: Research and Development Seminar 2010Malaysia, 2010.

[129] H. Fujii, C. Nakaya, H. Takeuchi, T. Kondo, Y. Ishikawa, Acoustic Properties of Lens Materials for Ultrasonic Probes, Japanese Journal of Applied Physics, 34 (1995) 312.

[130] Z. Li, S. Yang, M. Zhou, C. Hou, D. Chen, C. Fei, D. Li, Y. Quan, Y. Yang, Optimization design of autofocusing metasurface for ultrasound wave application, Journal of Advanced Dielectrics, (2022) 2350001.

[131] Z. Li, S. Yang, D. Wang, H. Shan, D. Chen, C. Fei, M. Xiao, Y. Yang, Focus of ultrasonic underwater sound with 3D printed phononic crystal, Applied Physics Letters, 119 (2021) 073501.

[132] H. Sun, S. Wang, S. Huang, L. Peng, Q. Wang, W. Zhao, Design and characterization of an acoustic composite lens with high-intensity and directionally controllable focusing, Scientific Reports, 10 (2020) 1469.

[133] Z. Li, R. Guo, C. Fei, D. Li, D. Chen, C. Zheng, R. Wu, W. Feng, Y. Yang, Liquid lens with adjustable focus for ultrasonic imaging, Applied Acoustics, 175 (2021) 107787.

[134] Z. Li, J. Zhao, C. Hou, C. Fei, C. Zheng, L. Lou, D. Chen, D. Li, Y. Yang, High-Frequency Self-Focusing Ultrasonic Transducer With Piezoelectric Metamaterial, IEEE Electron Device Letters, 43 (2022) 946-949.

[135] Z. Li, R. Guo, D. Chen, C. Fei, X. Yang, D. Li, C. Zheng, J. Chen, R. Wu, W. Feng, Z. Xu, Y. Yang, An Efficient Optimization Design of Liquid Lens for Acoustic Pattern Control, IEEE Transactions on Ultrasonics, Ferroelectrics, and Frequency Control, 68 (2021) 1546-1554.

[136] Z. Li, S. Yang, C. Fei, R. Guo, D. Chen, C. Zheng, Y. Yang, Adjustable Acoustic Field Controlled by "Ultrasonic Projector" on Ultrasound Application, IEEE Transactions on Ultrasonics, Ferroelectrics, and Frequency Control, 69 (2022) 254-260.

[137] Z. Li, D. Wang, C. Fei, P. Jiang, S. Zhang, D. Chen, D. Li, C. Zhen, R. Wu, X. Peng, Y. Xu, Z. Chen, W. Feng, Y. Yang, Acoustic Hole-Hologram for Ultrasonic Focusing With High Sensitivity, IEEE Sensors Journal, 21 (2021) 8935-8942.

[138] Z. Li, C. Fei, S. Yang, C. Hou, J. Zhao, Y. Li, C. Zheng, H. Wu, Y. Quan, T. Zhao, D. Chen, D. Li, G. Niu, W. Ren, M. Xiao, Y. Yang, Coding Piezoelectric Metasurfaces, Advanced Functional Materials, 32 (2022) 2209173.

[139] B. Salmon, D. Le Denmat, Intraoral ultrasonography: development of a specific high-frequency probe and clinical pilot study, Clinical Oral Investigations, 16 (2012) 643-649.

[140] J. Marotti, S. Heger, J. Tinschert, P. Tortamano, F. Chuembou, K. Radermacher, S. Wolfart, Recent advances of ultrasound imaging in dentistry – a review of the literature, Oral Surgery, Oral Medicine, Oral Pathology and Oral Radiology, 115 (2013) 819-832.

[141] C. Shi, X. Luo, J. Guo, Z. Najdovski, T. Fukuda, H. Ren, Three-Dimensional Intravascular Reconstruction Techniques Based on Intravascular Ultrasound: A Technical Review, IEEE Journal of Biomedical and Health Informatics, 22 (2018) 806-817.

[142] C. Fei, Y. Yang, F. Guo, P. Lin, Q. Chen, Q. Zhou, L. Sun, PMN-PT Single Crystal Ultrasonic Transducer with Half-concave Geometric Design for IVUS Imaging, IEEE Transactions on Biomedical Engineering, (2018) 1-1.

[143] J. Chen, C. Fei, D. Lin, P. Gao, J. Zhang, Y. Quan, D. Chen, D. Li, Y. Yang, A Review of UltraHigh Frequency Ultrasonic Transducers, Frontiers in Materials, 8 (2022).

[144] K.A. Snook, Z. Jian-Zhong, C.H.F. Alves, J.M. Cannata, C. Wo-Hsing, R.J. Meyer, T.A. Ritter, K.K. Shung, Design, fabrication, and evaluation of high frequency, single-element transducers incorporating different materials, IEEE Transactions on Ultrasonics, Ferroelectrics, and Frequency Control, 49 (2002) 169-176.

[145] J. Sauvage, M. Flesch, G. Férin, A. Nguyen-Dinh, J. Porée, M. Tanter, M. Pernot, T. Deffieux, A large aperture row column addressed probe for in vivo 4D ultrafast doppler ultrasound imaging, Physics in Medicine & Biology, 63 (2018) 215012.

[146] H. Hu, H. Huang, M. Li, X. Gao, L. Yin, R. Qi, R.S. Wu, X. Chen, Y. Ma, K. Shi, C. Li, T.M. Maus, B. Huang, C. Lu, M. Lin, S. Zhou, Z. Lou, Y. Gu, Y. Chen, Y. Lei, X. Wang, R. Wang, W. Yue, X. Yang, Y. Bian, J. Mu, G. Park, S. Xiang, S. Cai, P.W. Corey, J. Wang, S. Xu, A wearable cardiac ultrasound imager, Nature, 613 (2023) 667-675.

[147] M.Z. Nasrabadi, H. Tabibi, M. Salmani, M. Torkashvand, E. Zarepour, A comprehensive survey on non-invasive wearable bladder volume monitoring systems, Medical & Biological Engineering & Computing, 59 (2021) 1373-1402.

[148] X. Xue, B. Zhang, S. Moon, G.-X. Xu, C.-C. Huang, N. Sharma, X. Jiang, Development of a Wearable Ultrasound Transducer for Sensing Muscle Activities in Assistive Robotics Applications, Biosensors, 13 (2023) 134.

[149] H.-T. Oh, H.-J. Joo, M.-C. Kim, H.-Y. Lee, Effect of Mn on Dielectric and Piezoelectric Properties of 71PMN-29PT [71Pb(Mg1/3Nb2/3)O3-29PbTiO3] Single Crystals and Polycrystalline Ceramics, J. Korean Ceram. Soc, 55 (2018) 166-173.

[150] K. Song, Q. Li, H. Guo, Q. Hu, Z. Li, F. Li, S. Fan, Z. Xu, Composition and electrical properties characterization of a 5" diameter PIN-PMN-PT single crystal by the modified Bridgman method, Journal of Alloys and Compounds, 851 (2021) 156145.

[151] C.T.S. Corporation, The list of Piezoelectric Material Properties from CTS, https://www.ctscorp.com/wp-content/uploads/CTS-Piezoelectric-Material-Properties_Full-List_July21.pdf.

[152] W. Long, F. Guo, P. Fang, A. He, X. Li, Z. Xi, Temperature-dependent structure and electromechanical properties of Er doped PMN-PT single crystal grown by modified Bridgman technique, Journal of Alloys and Compounds, 902 (2022) 163858.

[153] https://info.piezo.com/hubfs/Data-Sheets/piezo-material-properties-data-sheet-20201112.pdf.

[154] K.K. Shung, Diagnostic Ultrasound: Imaging and Blood Flow Measurements, 2nd ed. ed., CRC Press, Place Published, 2015.

[155] W.R. Hedrick, D.L. Hykes, Beam Steering and Focusing With Linear Phiased Arrays, Journal of Diagnostic Medical Sonography, 12 (1996) 211-215.

[156] A.H. Aitkenhead, J.A. Mills, A.J. Wilson, The Design and Characterization of an Ultrasound Phased Array Suitable for Deep Tissue Hyperthermia, Ultrasound in Medicine & Biology, 34 (2008) 1793-1807.

[157] M. Kim, J. Kim, W. Cao, Aspect ratio dependence of electromechanical coupling coefficient of piezoelectric resonators, Applied Physics Letters, 87 (2005) 132901.

[158] H. Kim, S. Lee, Characterization of Electrical Heating of Graphene/PLA Honeycomb Structure Composite Manufactured by CFDM 3D Printer, Fashion and Textiles, 7 (2020) 8.

[159] B. Panda, M. Leite, B.B. Biswal, X. Niu, A. Garg, Experimental and numerical modelling of mechanical properties of 3D printed honeycomb structures, Measurement, 116 (2018) 495-506.

[160] M. Akram, M. Iqbal, M. Daniyal, A.U. Khan, Awareness and current knowledge of breast cancer, Biological Research, 50 (2017) 33.

[161] M.S. Essa, M.H. Faheem, R. Abdalla, M.E. Zayed, The relationship between distance of breast cancer from the skin and incidence of axillary nodal metastasis in female patients with early cancer breast: correlation between radiological and pathological distance, The Egyptian Journal of Surgery, 40 (2021).

[162] C.V. Nguyen, R.F. Saraf, Tactile Imaging of an Imbedded Palpable Structure for Breast Cancer Screening, ACS Applied Materials & Interfaces, 6 (2014) 16368-16374.

[163] M. Mance, K. Bulic, A. Antabak, M. Miloševic, The influence of size, depth and histologic characteristics of invasive ductal breast carcinoma on thermographic properties of the breast, EXCLI Journal, 18 (2019) 549-557.

[164] https://ameultrasounds.com/products/ge-ml6-15-d-linear-array-probe.